UNIVERSITÀ DEGLI STUDI DI PADOVA

Dipartimento di Fisica e Astronomia “Galileo Galilei”

Master Degree in Physics

Final Dissertation

Study of the ^{12}C(p,γ)^{13}N at astrophysical energies at LUNA

Thesis supervisor	Candidate
Dr. Antonio Caciolli	Jakub Skowronski

Academic Year 2019/2020

Abstract

The ^{12}C/^{13}C ratio is a sensitive indicator of the degree of stellar nucleosynthesis and thus it can be used as a tracer of galactic chemical evolution. Nevertheless, the C isotopic ratio variation after the dredge-up phenomenons occuring in Asymptotic Giant Branch (AGB) and Red Giant Branch (RGB) stars is highly dependant on the adopted rate for the proton capture reaction on ^{12}C.

In a *RGB* star, the Gamow peak of the reaction lies between 20 and 70 keV. Given the exponential drop of the cross section, the reactions at such low energies are very difficult to measure because of the very low signal counting rate. Nevertheless, a precise measurement of the $^{12}C(p,\gamma)^{13}N$ reaction magnitude is necessary to make reliable predictions about the evolution of *RGB* stars. On the contrary, the Gamow peak for an *AGB* stars lies between 50 and 150 keV. This energy range can be measured through the detection of prompt γ-rays.

Measurements of the $^{12}C(p,\gamma)^{13}N$ reaction cross section were performed at the Laboratory for Underground Nuclear Astrophysics (LUNA), located at the Labaratori Nazionali del Gran Sasso (LNGS) in Italy. Being located underground, the γ-ray background is suppressed by more than three orders of magnitude, thus providing a unique environment for low-energy measurements of reaction cross sections.

Prompt γ-rays associated with the formation of ^{13}N nuclei were analysed to determine the non-resonant contribution to the reaction cross section. The total non-resonant S-factor was determined at energies between $E_{\mathrm{cm}} \approx 75 - 350$ keV, obtained with great precision. Nevertheless, the preliminary results are discordant with the literature data. The reason of such a discrepancy is still unkown and has to be understood in future analysis.

Contents

Introduction

During the 14 billon years since the Big Bang, from which the origin of our Universe is traced, a uniquely complex system of evolutionary processes has occured. These events, including the creation of galaxies, stars, planetary bodies and their constituent elements, have been vital precursors to the formation of our planet. In addition, nuclear processes occuring inside the star interiors are crucial for the production of energy radiated from the stellar surface and for the synthesis of the elements.

In particular, the CNO cycle is of exceptional importance. First of all, it is the main source of energy for the stars approximately 1.2 times bigger than our Sun. Secondly, even though the energy contribution for the smaller stars is negligible, the consequences on the nucleosynthesis are crucial. In fact, the CNO equilibrium regulates the ratios of the different isotopes, e.g. the ^{12}C/^{13}C ratio.

This thesis is focused on the experimental investigation of the first reaction of the CNO cycle, the $^{12}\mathrm{C}(p,\gamma)^{13}\mathrm{N}$. This reaction has important consequences during the convective mixing episodes occuring inside the stars when they start either their Red Giant Branch or Asymptotic Giant Branch phases. These events, called respectively first and third dredge-up, change drastically the ratios of several different isotopes present inside the stellar atmosphere as the convective motion mixes the CNO products with the external regions of the star. Recently, deviations from the calculated abundances were observed in the atmospheres of globular cluster giants [1]. Moreover, the study of isotope abundances in carbonaceous chondrite meteorites, which are thought to be formed inside carbon stars atmosphere, produces some puzzling results [2]. Thus, it is mandatory to reduce the uncertainties affecting the $^{12}\mathrm{C}(p,\gamma)^{13}\mathrm{N}$ reaction rate in order to better constrain the possible mixing phenomena.

The experiment was conducted at LNGS underground laboratories in November/December 2019. The unique low background environment of LNGS permits to measure extremely weak processes at astrophysical energies with an excellent precision. The proton beam coming from the LUNA 400kV accelerator was directed on thin ^{12}C targets, produced by evaporation on Ta backings. An HPGe detector of 104% relative efficiency was used to detect the prompt γ-rays coming from the $^{12}\mathrm{C}(p,\gamma)^{13}\mathrm{N}$ reaction. This thesis reports preliminary S-factor obtained in the proton energy range between 80 and 370 keV. A detailed evaluation of systematic uncertainties is still in progress.

The thesis is organized in the following way: Chapter 1 provides a brief introduction to stellar evolution and the nucleosynthesis processes. An introduction to the dredge-up events is also presented, the reaction mechanism of the $^{12}\mathrm{C}(p,\gamma)^{13}\mathrm{N}$ is explained and the state of art of the reaction is discussed. In Chapter 2, the importance of the background reduction at the LNGS laboratory is illustrated, and the experimental setup used during the experiment is outlined. Chapter 3 reports the analysis and results of this investigation.

Chapter 1

Astrophysical Motivation

Nuclear reactions are crucial for astronomy and astrophysics. Almost all of the visible light from our galaxy comes as a product of the different reactions occuring in the stars [3]. In fact, the fusion of light elements into heavier ones is usually an exothermic process that liberates energy in form of radiation, which is essential to sustain them during their life. As almost all of the elements located not only on Earth, but also in our Solar System and in our Galaxy, were created inside the hot interiors of these celestial bodies [4], it is necessary to study thermonuclear reactions taking place inside stellar cores, in order to be able to reconstruct the stellar history and, consequently, the history of the Universe. One of these is the $^{12}\mathrm{C}(p,\gamma)^{13}\mathrm{N}$ reaction which affects the abundance of $^{12}\mathrm{C}$, one of the most abundant elements in our bodies, as well as the $^{12}\mathrm{C}/^{13}\mathrm{C}$ isotopic ratio.

In the first section, I will elaborate over the concept of nucleosynthesis, including a brief description of the life cycle of a star, and illustrate the problem regarding the $^{12}\mathrm{C}/^{13}\mathrm{C}$ abundances ratio. Next, I will introduce the formalism of non-resonant reactions occuring in the star interiors. Finally, I will present the state of art of the $^{12}\mathrm{C}(p,\gamma)^{13}\mathrm{N}$ reaction.

1.1 Nucleosynthesis

The abundances of naturally occurring nuclides are reasonably well known. In particular, the abundances in the Solar System are shown in Fig. 1.1. It is then natural to ask what accounts for their different occurences in our Universe and which are the processes that produced these elements. This is the main goal of the studies regarding *nucleosynthesis*.

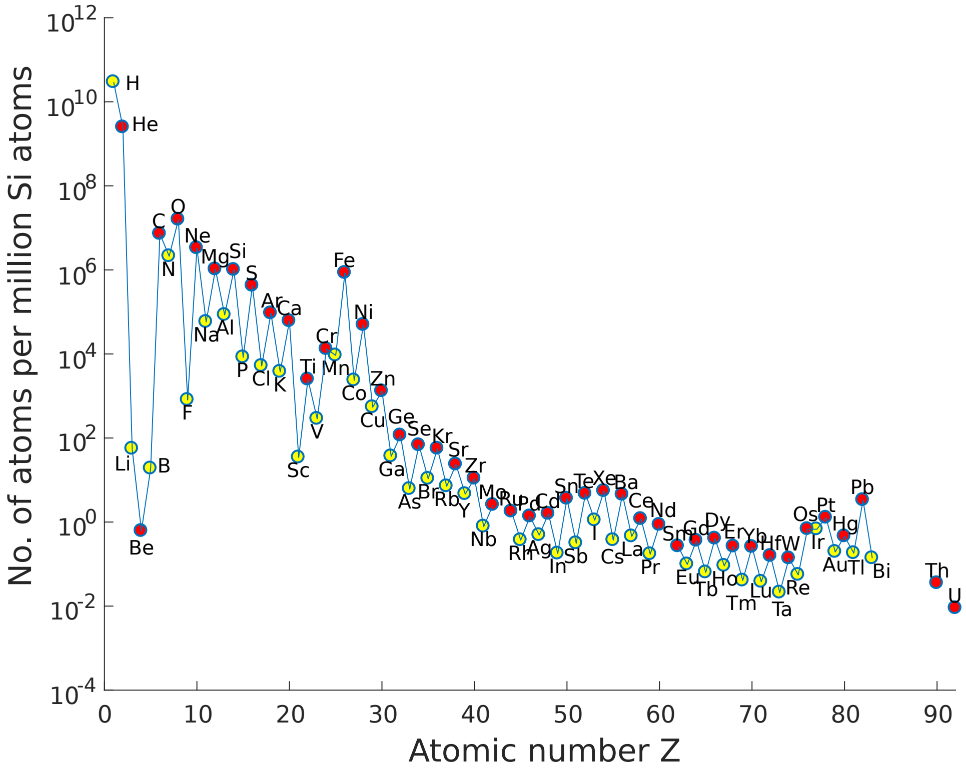

Figure 1.1: Abundances of the elements in the Solar System as a function of atomic number. The red and yellow points represent respectively even and odd nuclei. The data were taken from [5].

At first, scientists thought the nucleosynthesis primarily occured during the Big Bang [6]. None of these theories, however, could successfully describe the observations. After the failure to find a single mechanism that could explain the observed abundance of nuclides, a new view arose. It relied on a number of different reactions, operating in different environments and at different times in the history of the Universe. These reactions gave origin to the elements in the current abundances. This theory, also called the *Polygenetic Hypothesis*, was formalized by the work of Burbidge, Burbidge, Fowler and Hoyle [4].

The polygenetic hypothesis proposes four phases of nucleosynthesis: Cosmological Nucleosynthesis, Stellar Nucleosythesis, Explosive Nucleosythesis and Galactic Nucleosythesis.

Cosmological Nucleosynthesis occurred shortly after the Big Bang and is responsible for the cosmic abundance of H and He, and some of the Li. Stellar Nucleosythesis began after the creation of first stars. In fact, especially during the advanced stages of massive stars evolution, stellar fusion accounts both for the abundances of lighter elements, up to and including Si, and, in a smaller part, for the abundances of heavier elements. In addition, in massive stars the s-process partially accounts for the abundances in $Z > 26$ region. The synthesis of the remaining elements occurs when large stars exhaust their nuclear fuel and explode forming a supernova (Explosive Nucleosynthesis). Finally, Li and Be are continuously produced in the interstellar space by interaction of cosmic rays with matter: this process is called Galactic Nucleosynthesis.

This thesis focuses on stellar nucleosynthesis. In particular, the ^{12}C/^{13}C abundances ratio will be discussed. Beforehand, however, a brief description of stellar evolution is presented.

1.1.1 The Evolution of Stars

Stellar life is driven by nuclear fusion processes, which maintain the stellar geometrical structure thanks to the pressure they generate. In fact, as the gravitation is continuously trying to collapse the star, the internal pressure, generated by nuclear reactions inside the stellar core, acts in the opposite way. The spherical form we observe is the immediate result of the equilibrium reached by the two forces.

At the initial stages of its life, the star burns its lightest element, ^{1}H. In fact it is the most abundant element occuring in protostellar nebulas. In addition, it has the lowest Coulomb barrier, which must be overcome by the nuclear fusion process. This stage is referred to as *hydrogen burning.* During this period, two main processes are possible for the star energy production: the *pp* chain [7] and *CNO* cycle [8]. They are visualized in Fig. 1.2 and Fig. 1.3. Both of these convert four ^{1}H nuclei into one ^{4}He nucleus, generating large amounts of energy, given by the mass difference between the initial and final states. The predominance of one process over the other depends strongly on the star temperature, and on its initial compositon: in fact, the *pp* chain is dominant for stars with low masses, where the core temperature is lower than 20 million degrees Kelvin [9]. The *CNO* cycle, instead, is the predominant source of energy for massive stars. In addition, the latter is only possible if C, N and O nuclei were present in the initial protostellar nebula from which the star has been formed. In fact, the *CNO* is mainly occuring in second generation stars which were ignited from the remnants of a previous supernova. Nevertheless, at this point of the stellar life cycle, no reactions produce stable elements heavier than ^{4}He.

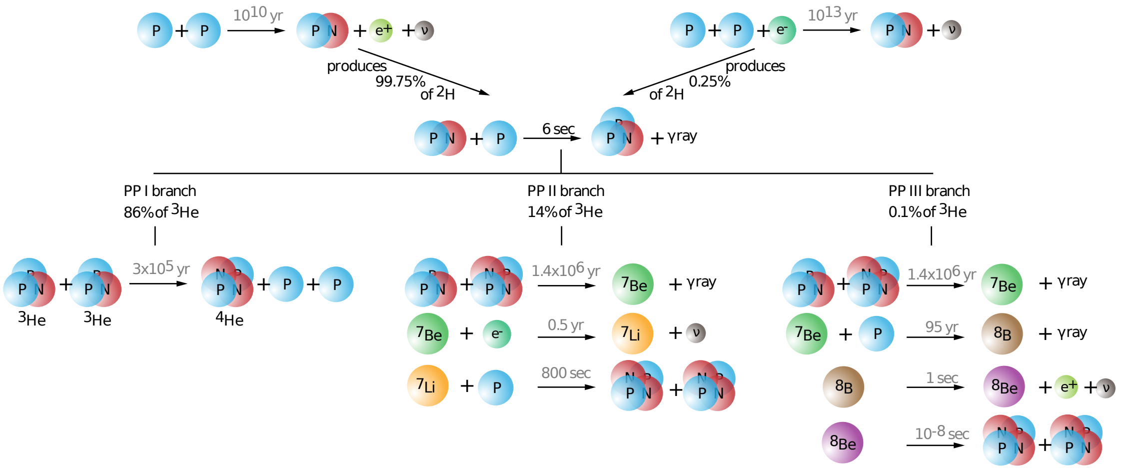

Figure 1.2: Scheme of the *pp* chain reactions. More than one chain is possible depending on the stellar temperatures. [10]

When the amount of hydrogen decreases and consequently its burning rate is not high enough to counterbalance the gravitational force, the star shrinks and its core temperature rises until the new equilibrium is reached. In the same moment, due to higher core density and higher temperatures, new nuclear reactions start in the core, proceeding at higher rates than the hydrogen burning ones, which are therefore transferred to an outer shell of the star. This stage is called the *helium burning* phase. In fact, during this period, the so-called triple-alpha reaction is the main source of the stellar energy production [11]. Two ^{4}He nuclei fuse to form a ^{8}Be nucleus, but this, being highly unstable, rapidly decays to two ^{4}He nuclei again. Very rarely, however, a third helium nucleus can be added to ^{8}Be before it decays, forming a nucleus of ^{12}C. This is permitted by the large abundance of ^{4}He, created by the hydrogen burning phase, by the increased temperatures of the stellar core and by the presence of the resonant state of the ^{12}C nuclei, called the Hoyle state. In this way, the probabilty that a third ^{4}He nuclei interacts with the newly created ^{8}Be before it decays is high enough to make it the main thermonuclear reaction in the stellar core at this point of the stellar evolution.

After this stage, stars with mass lower then $\sim 8M_\odot$ usually end their life cycle and leave a small and dense core, which is called the White Dwarf. If the star is massive enough, however, several other burning stages are possible, producing heavier and heavier elements. The stopping point are the Fe and Ni nuclei, in the A $\sim$ 60 region. In fact, the fusion of nuclei to build heavier elements becomes an endothermic process, as the binding energies per nucleon start to decrease. This is

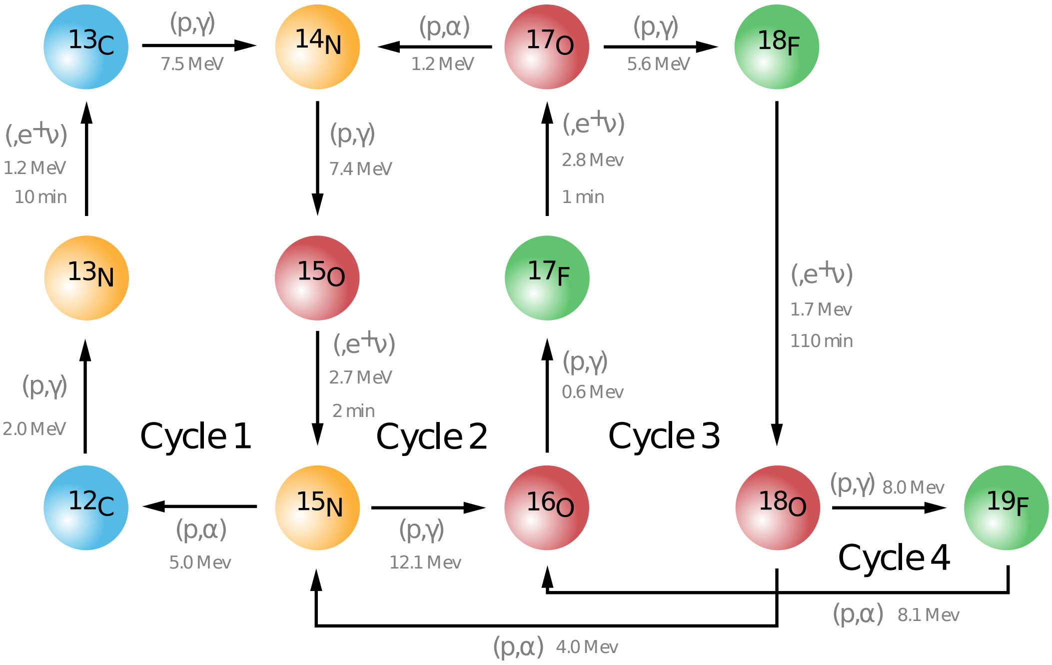

Figure 1.3: Scheme of the *CNO* cycle reactions. Different cycles can be created depending on the stellar core temperatures. [10]

crucial for the star evolution as no more energy can be obtained from the fusion, and thus its life cycle ends. At this point, the star collapses and then explodes violently, becoming a supernova and turning into either a Neutron Star or a Black Hole.

1.1.2 The ^{12}C and ^{13}C Abundances Problem

The $^{12}\mathrm{C}(p,\gamma)^{13}\mathrm{N}$ reaction takes part in the *CNO* cycle of hydrogen burning. The cycle is active during the main sequence, *RGB* and *AGB* phases. Being a catalytic cycle, it not only converts 4 protons into one helium nucleus, but also governs the abundances of the C, N and O isotopes that take part in the cycle. One of the most important isotopic abundance ratios is the $^{12}\mathrm{C}/^{13}\mathrm{C}$ one. It is a sensitive indicator of the degree of stellar nucleosynthesis and thus is used as a tracer of galactic chemical evolution [12]. While ^{12}C is produced in helium burning by the triple-alpha process, ^{13}C is produced by the $^{12}\mathrm{C}(p,\gamma)^{13}\mathrm{N}$ reaction and the subsequent β^+ decay to ^{13}C. *RGB* and *AGB* stars are then able to effectively enrich the interstellar medium with hydrogen burning products, thanks to the combination of mixing phenomena and intense stellar winds.

The *RGB* phase starts when the star exhausts most of its hydrogen fuel. Initially, the stellar core, mainly made of ^{4}He, is inert and all of the energy produced by the star comes from the hydrogen burning, which is transported to an outer shell. In the same moment, the so-called first dredge-up [13] occurs, a convective mixing episode that brings material from inner layers previously processed by the *CNO* cycle to the star surface. As a consequence of this event, the surface C abundance decreases, as well as the ^{12}C/^{13}C ratio. During this phase, the hydrogen shell burning occurs at $\sim 30 - 50$ MK [14].

The *AGB* phase starts when the degenerate core is predominantly made of C and O, and a thin helium burning shell surrounds the C-O core. When most of the ^{4}He fuel in the shell is exhausted, the star begins deriving its energy from fusion of hydrogen in a thin shell. The helium from the hydrogen shell burning builds up and eventually the helium shell ignites again. In the same moment, the region between the two shells becomes unstable to convection for a short period, the external layers expand and the hydrogen shell burning temporarily stops. As a consequence, the convective envelope penetrates into the C-rich and H-exhausted layers, bringing the freshly synthesized nucleosynthesis products to the surface. This is referred to as the third dredge-up [15, 16], and is visualized in Fig. 1.4. This leads to an increase in the ^{12}C/^{13}C ratio inside the star atmosphere. In addition, this process is repeated several times until the star expands enough to ignite the carbon burning in the core. During this phase, the *CNO* cycle burns at temperatures up to ~ 100 MK [14].

The ^{12}C/^{13}C ratio in the Solar System is estimated to be of about 90 [17]. One of the possible origins for the elements in the Solar System are the Asymptotic Giant Branch stars [18], which are incredibly prolfilic centers of nucleosynthesis. Nevertheless, more insight of the mixing phenomena occurring inside these stars is needed in order to allow more precise predictions.

The observation of *RGB* stars with masses $M < 2.5 M_\odot$ in the Milky Way and in the Magellanic Clouds indicates smaller ^{12}C/^{13}C ratios ($\sim$ 6 - 18) [1, 19] than the ones predicted from the *RGB* star models. A generally accepted explanation for such a discrepancy is the presence of new mixing processes which does not depend on the convective motion inside the star. The possible sources could be the angular momentum of the star [20], magnetic buoyancy [21] or gravitional waves [22]. In addition, such ratios were also found by analyzing the SiC grains of the pristine meteorites [2]. These are formed in the atmosphere of *AGB* stars, and thus should give a reliable hint about the star surface composition.

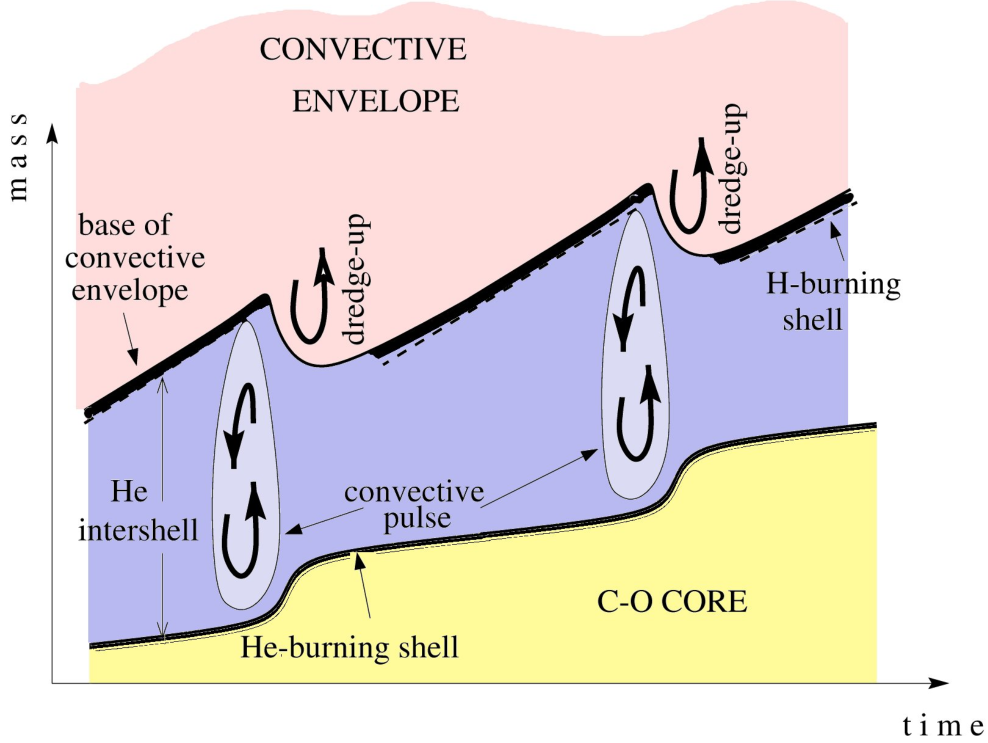

Figure 1.4: Scheme representing the typical structure for AGB stars. The convective pulses transport the produced elements through the different layers of the star, altering their abundances.

Obviously, the C isotopic ratio variation after the *dredge-up* phenomena depends highly on the adopted rates of proton capture reactions for both ^{12}C and ^{13}C. Hence, a precise measurement of the magnitude of these reaction is necessary to make reliable predictions about the *RGB* and *AGB* stars evolution.

1.2 Thermonuclear Reactions in Stars

In order to understand how nuclear reactions contribute to stellar evolution and nucleosynthesis it is necessary to introduce the reaction rate formalism. The starting point is the definition of the cross section, σ. This observable describes the probability that a given reaction will take place. Let's consider the following reaction:

$$a + X \rightarrow Y + b \tag{1.1}$$

where $a + X$ is the entrance channel and $Y + b$ is the exit channel. It is possible to define the reaction rate, r_{aX}, for this process as follows:

$$r_{aX} = N_a N_X v\sigma(v) \tag{1.2}$$

where r_{aX} is the number of reactions that occured per unit time and volume, N_a and N_X are the number densities of particles a and X respectively. The cross section, $\sigma(v)$, is written explicitly as a function of v, the relative velocity between the two entrance channel particles. The stellar plasma can be, in good approximation, modelled as an ideal gas, which consists of a mix of free non-interacting particles. Moreover, it is assumed to be fully ionized; the temperature in the stellar interiors, in fact, is high enough to make it a reasonable assumption. As such, the relative velocities between its particles follows the Maxwell-Boltzmann distribution $\phi(v)$:

$$\phi(v) = 4\pi v^2 \Big(\frac{\mu}{2\pi kT}\Big)^{\frac{3}{2}} \exp\Big(-\frac{\mu v^2}{2kT}\Big) \tag{1.3}$$

where μ is the reduced mass of the two particles system, k is the Boltzmann constant and T denotes the stellar temperature. Alternatively, $\phi(v)$ can be expressed in terms of kinetic energy, E, as:

$$\phi(E) \propto \exp\Big(\frac{E}{kT}\Big)E \tag{1.4}$$

Now, it is possible to define the *reaction rate*, $\langle\sigma v\rangle_{aX}$, through the following:

$$\begin{aligned} r_{aX} &= N_a N_X \int_0^\infty \phi(v) v\sigma(v) dv && (1.5) \\ &= N_a N_X \langle\sigma v\rangle_{aX} && (1.6) \end{aligned}$$

Inserting the Maxwell-Boltzmann distribution into the previous equation, the reaction rate per particle pair becomes:

$$< \sigma v >_{aX} = \Big(\frac{8}{\pi\mu}\Big)^{\frac{1}{2}} \frac{1}{(kT)^{\frac{3}{2}}} \int_0^\infty \exp\Big(-\frac{E}{kT}\Big)\sigma(E)EdE \tag{1.7}$$

The reaction rate is one of the most important variables in nuclear astrophysics. In fact it determines completely the importance of a specific reaction in the stellar environment: it incorporate both the information about the reaction itself, through its cross section, and about the energy distribution of the particles that participate in the reaction, through the Maxwell-Boltzmann distribution.

In order to proceed, the reaction cross section, σ, must be found. To accomplish that, it is necessary to discuss the properties of the ^{12}C$(p,\gamma)^{13}$N reaction.

1.2.1 The ^{12}C$(p,\gamma)^{13}$N Reaction

The ^{12}C$(p,\gamma)^{13}$N reaction can proceed through two strong resonant states located at proton energies of 457 keV and 1699 keV, with a subsequent γ-ray emission to the ^{13}N ground state or via the non-resonant component. The energy range of astrophysical interest lies between 30 keV and 150 keV (Fig. 1.7 and Fig. 1.8). At these energies, the cross section is dominated by the non resonant component and the tail of the 457 keV resonance.

The ^{13}N nucleus is formed directly in ground state from the entrance channel (p + ^{12}C). This nuclear process is combined with a γ-ray emission, which must conform to the energy conservation. In fact, the energy of the emitted γ-ray, E_γ, is:

$$E_\gamma = Q_{\text{value}} + E_{\text{CM}} \tag{1.8}$$

where the Q_{value} is the Q-value of the reaction, and E_{CM} is the energy of the incoming proton in the Center of Mass (CM) frame. The level scheme depicting the reaction is shown in Fig. 1.5.

Let's consider the DC reaction in more details: the charged particle, p, must posses sufficient energy to overcome the potential barrier created by the presence of the target nucleus, ^{12}C. There are two main components for the barrier: the Coulomb potential and the centrifugal barrier, associated to the relative angular momentum.

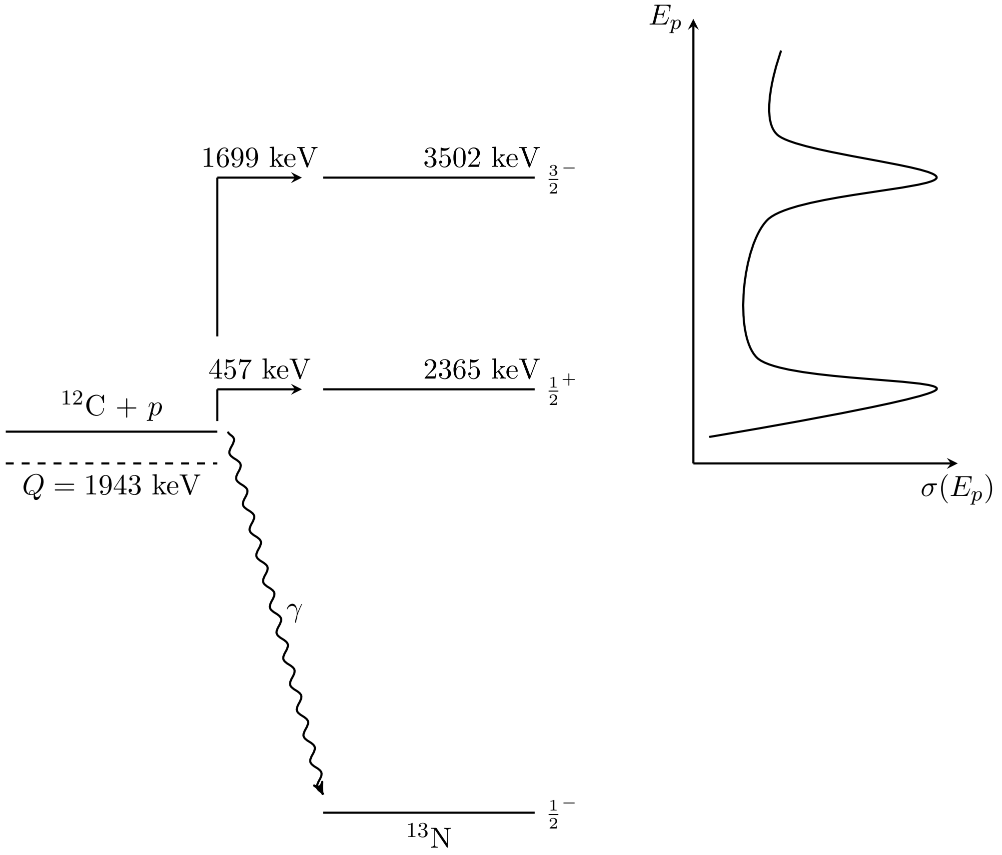

Figure 1.5: The level scheme of the $^{12}\mathrm{C}(p,\gamma)^{13}\mathrm{N}$ reaction. The Q-value of the reaction is 1943.5(2) keV. On the right, an approximated cross section of the reaction is plotted.

The Coulomb potential experienced by the two particles, of charge Z_p and $Z_{^{12}\mathrm{C}}$, separated by a distance r of the order of the nuclear radius, is given by:

$$V_{\mathrm{C}}(r) = \frac{Z_p Z_{^{12}\mathrm{C}} e^2}{4\pi\epsilon_0 R_{^{12}\mathrm{C}}} \approx 1 \text{ MeV} \tag{1.9}$$

where e is the elementary charge, ϵ_0 is the vacuum permittivity and $R_{^{12}\mathrm{C}}$ is the ^{12}C nuclear radius.

The centrifugal barrier between the two particles with relative orbital angular momentum l can be written as:

$$V_{\mathrm{cf}}(r) = \frac{l(l+1)\hbar^2}{2\mu r^2} \tag{1.10}$$

where $\hbar$ is the reduced Planck constant.

In addition, the strong nuclear force must be considered, as it accounts for the small range attraction between all the nucleons inside the nucleus. Unfortunately, there is no exact analytical form for its parametrization. For this reason, a square-well or a Woods-Saxon potential is often used to describe the potential action inside the nucleus. The overall situation, in $l = 0$ case and a square-well nuclear potential, is depicted in Fig. 1.6.

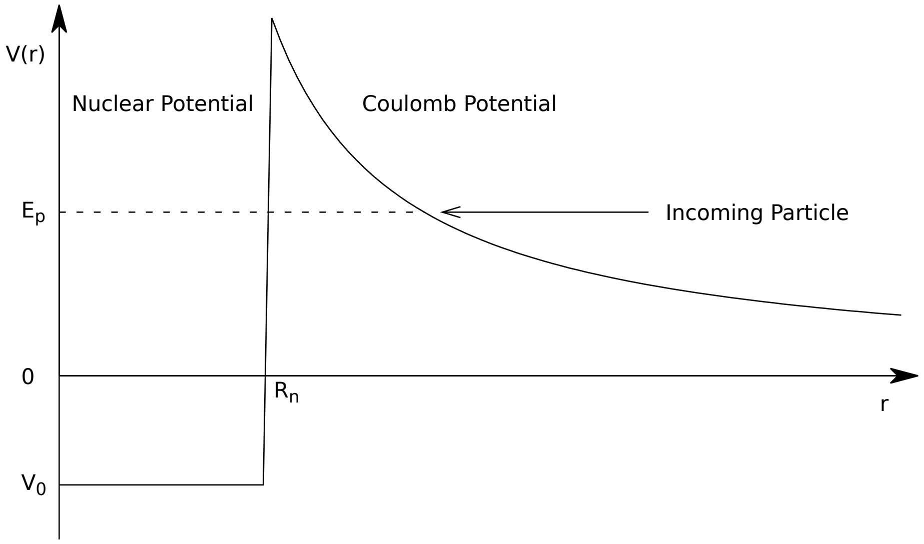

Figure 1.6: Schematic representation of the Coulomb barrier and the nuclear potential well. By overcoming the barrier, the projectile enters a zone ($r < R_n$) dominated by the strong force attraction.

In order to make the nuclear reaction possible, the interacting charged particles must acquire enough energy to overcome the potential barrier, which in case of s-wave ($l = 0$) has only the Coulomb contribution. From a quantum mechanical point of view, the barrier can be penetrated, even if the energy of the projectile in the CM frame, E_p, is lower than the barrier height. This phenomenon is called the *Quantum Mechanical Tunneling.* By taking this effect into account, the probability of penetrating the potential barrier is:

$$P_{\mathrm{G}} \propto \exp(-2\pi\eta) \tag{1.11}$$

where η is the Sommerfeld parameter, and the term $2\pi\eta$ can be written as:

$$2\pi\eta = 31.29 Z_p Z_{^{12}\mathrm{C}} (\frac{\mu}{E})^{\frac{1}{2}} \tag{1.12}$$

$$= 187.74 \left(\frac{\mu}{E}\right)^{\frac{1}{2}} \tag{1.13}$$

with the centre of mass energy E, given in units of keV, and reduced mass μ, in atomic mass units (amu).

In this case, the non-resonant cross section can be expressed in terms of the barrier penetrability as:

$$\sigma(E) = \frac{1}{E}\exp(-2\pi\eta(E))S(E) \tag{1.14}$$

where the term $1/E$ is associated to the de Broglie wavelength, λ. As the cross section must be extrapolated to low energies, the $S(E)$ is introduced. It is the astrophysical S-factor, which includes only the purely nuclear component of the cross section. In fact, being much smoother function of energy, it is easier to extrapolate to low energies.

It is possible to substitute Equation 1.14 into Equation 1.7, in order to obtain the reaction rate per particle pair for the non-resonant ^{12}C$(p,\gamma)^{13}$N reaction:

$$< \sigma v >_{p,^{12}C} = \left(\frac{8}{\pi\mu}\right)^{\frac{1}{2}} \frac{1}{(kT)^{\frac{3}{2}}} \int_0^\infty S(E)\exp\Big(-\frac{E}{kT} - 2\pi\eta(E)\Big)dE \tag{1.15}$$

where two different terms are present in the exponential: one which accounts for the Maxwell-Boltzmann energy distribution, the other considers the Coulomb barrier penetration probability.

The product of the two exponential terms in Equation 1.15 defines an energy window, called the Gamow window, in which the reaction is most likely to occur.

In fact, it is possible to differentiate this component and obtain the energy, E_0, corresponding to the maximum reaction rate at a given temperature. This energy is referred to as the Gamow peak. In Fig. 1.7 and Fig. 1.8 the Gamow peak is illustrated for the ^{12}C$(p, \gamma)^{13}$N reaction in typical *RGB* and *AGB* hydrogen burning shells at temperatures of 0.03 GK and 0.1 GK respectively.

It is clear that in both *AGB* and *RGB* stars, the DC component contributes strongly as the Gamow peak window falls below the first ^{13}N resonance. Its importance is even bigger for smaller stars, for which the Gamow peak window will lie in even lower energy region. Thus, a precise measurement of the S-factor at low energies is necessary in order to make reliable predictions about the evolution of ^{12}C abundances inside star interiors.

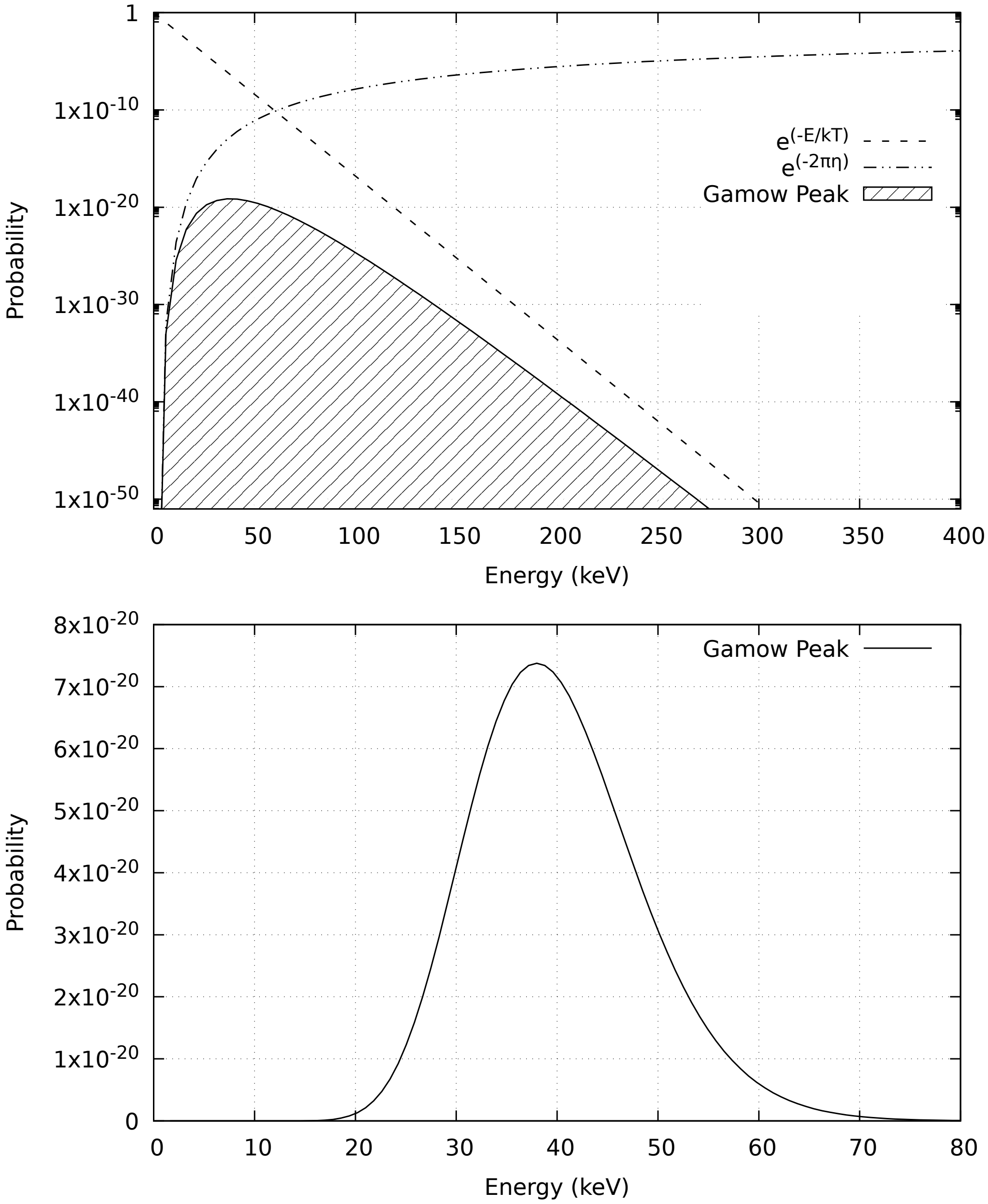

Figure 1.7: The Gamow peak (filled area) calculated for ^{12}C$(p,\gamma)^{13}$N reaction considering $T =$ 0.03 GK (*RGB* star). The two contributions are plotted with dashed lines. In the second figure, the Gamow peak is plotted in linear scale.

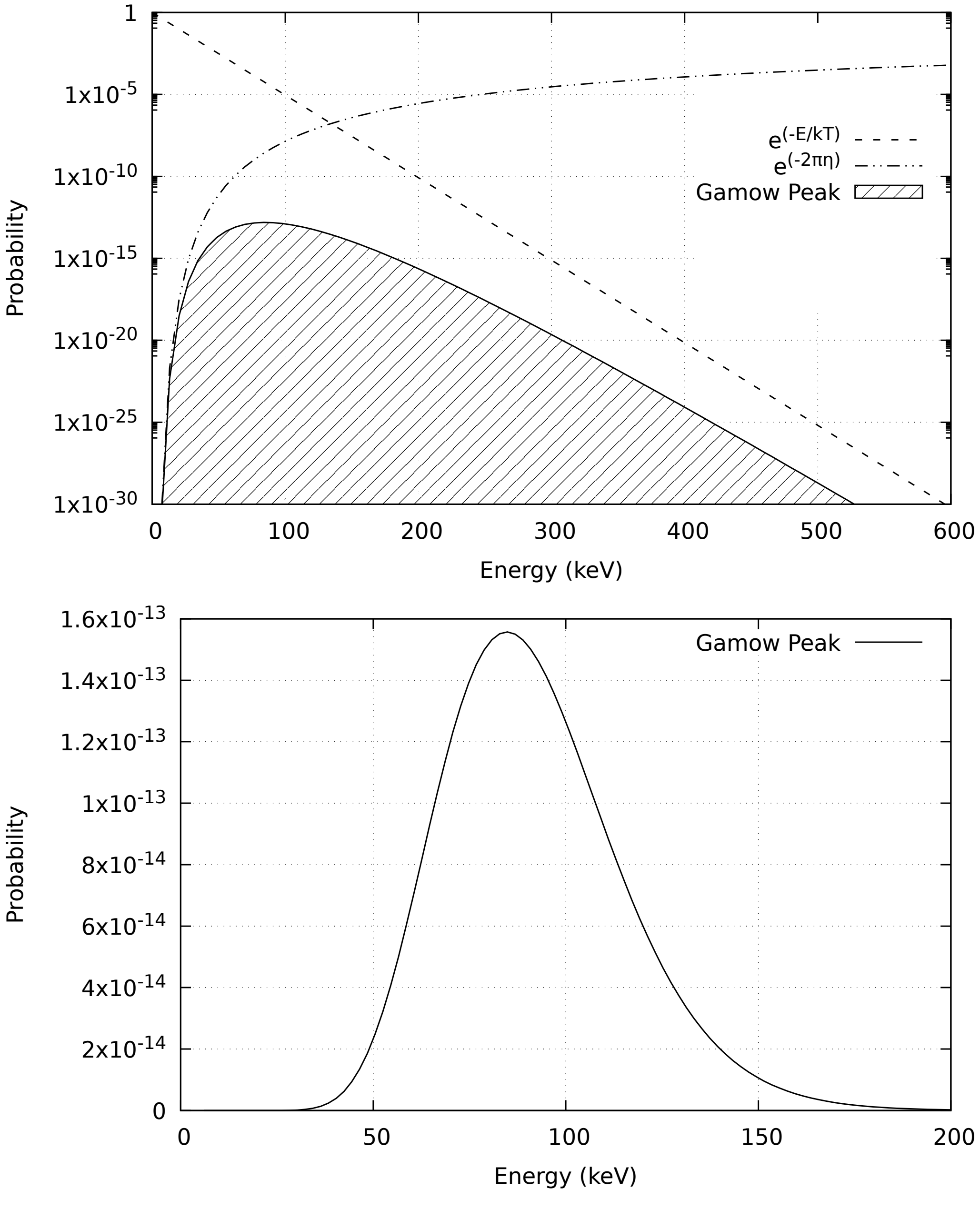

Figure 1.8: The Gamow peak (filled area) calculated for ^{12}C$(p,\gamma)^{13}$N reaction considering $T = 0.1$ GK (*AGB* star). The two contributions are plotted with dashed lines. In the second figure, the Gamow peak is plotted in linear scale.

1.3 Current Status of ^{12}C$(p,\gamma)^{13}$N Reaction

Several experiments were performed in the past in order to investigate the ^{12}C$(p,\gamma)^{13}$N reaction. These measurements, however, have not obtained great precisions as were made at around the dawn of the Polygenetic Hypothesis, when experimental setups were not able to achieve current reliability. In case of the *RGB* stars, the Gamow peak of the reaction lies at around 30 keV and it is not possible to study the reaction at such low energies, because of its extremely low cross section in this region. Hence, it is necessary to extrapolate the measured S-factor at low energies. This procedure is highly sensitive to errors of the measurement, thus high precision is needed to obtain a solid result. On the contrary, experimental data are available in the Gamow window for *AGB* stars.

In the following, the previous measurements of the reaction are presented:

- (1949) Baily [23] and Hall et al. [24] have simultaneusly performed two experiments for two different ranges of energy. The former measured the ^{12}C$(p,\gamma)^{13}$N cross section from 125 keV to 200 keV, using a thick carbon target (graphite). The results were obtained in an indirect way, by looking at the ^{13}N activity, which has a half-life of 10 minutes. By using such a methodology, it is possible that the measurement was affected, mainly at high energies, by the ^{13}N evaporation from the target, but no clear evidence were found of this effect. The latter experiment focused on the energies between 88 keV and 128 keV. As it was not possible to completely suppress the environmental background, a direct identification of the direct capture γ-ray at such low energies was unattainable. Thus, also in this case the indirect ^{13}N activity was used. Nevertheless, the counting rates measured were only slightly above background and many different factors contributed to the cross section error, which was evaluted to be about ± 20%.
- (1957) Lamb et al. [25] performed an experiment to measure the cross section of the reaction using beam energies from 80 keV to 126 keV. The observation was made directly by searching for the transition to ^{13}N ground state. The same energy window for the γ-spectrum was used for all the energies which made it vulnerable to background noise. In fact, the measurement is affected by substantial errors which ranges from ±13% to ±41%.
- (1963) J. Vogl [26] studied the reaction as a part of his PhD. thesis. The main focus of his work, however, was the ^{13}C$(p,\gamma)^{14}$N reaction. The measured

energy window ranged from 150 keV to 680 keV. The results obtained are in good agreement with the previous experiment, but the precision of the cross section at the lowest energies is poor: the measurement error ranges from 20% to 90% below 230 keV.

- (1974) Rolfs et al. [27] analyzed the ^{12}C$(p,\gamma)^{13}$N reaction. However, the focus of the experiment was put on the two ^{13}N excited states at 2365 keV and at 3502 keV. The measurement of the cross section was performed also down to proton energy of 150 keV. In addition, the reaction was considered both at $\theta = 0°$ and $\theta = 90°$. The analysis was also made for the elastic proton scattering ^{12}C$(p,p)^{12}$C reaction channel. The extrapolation of the S-factor resulted in good agreement with the previously qutoed works, with the precision of 14%.

The plot of S-factor versus the center of mass energy for the ^{12}C$(p,\gamma)^{13}$N reaction is presented in Fig. 1.9, where all the different literature data are compared, with the exception of Fowler et al. data, as they are not provided in any database. As the data were originally provided in form of the cross section σ, the points were transformed into S-factors using Equation 1.14. As can be seen in Fig. 1.9, a large part of the Gamow window is still unexplored. Moreover, there is poor energy overlap between different data sets.

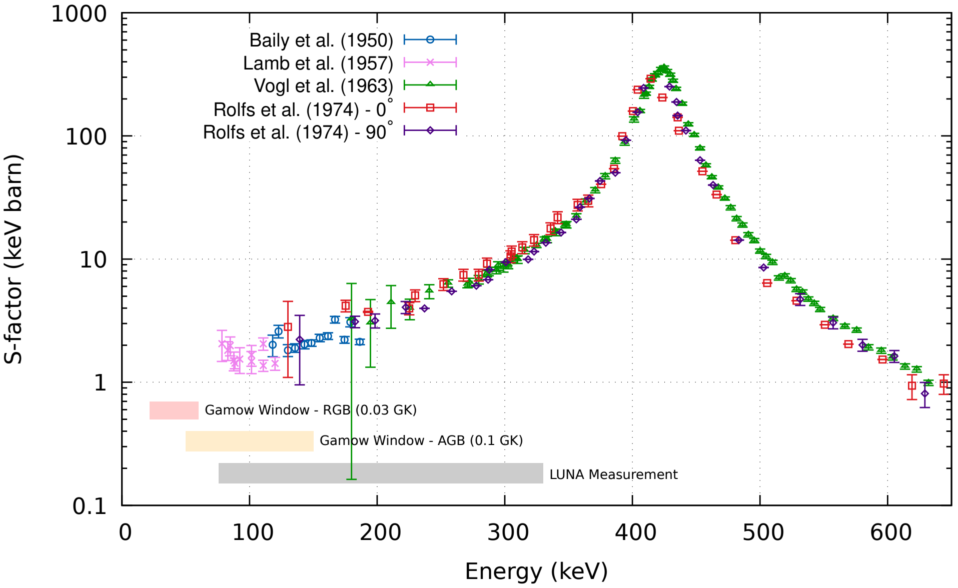

Figure 1.9: Comparison of results for most of the literature data. Gamow windows for the *AGB* and *RGB* stars are highlighted. In addition, the energy range measured at LUNA is shown.

Chapter 2

Experimental Setup

Given the exponential drop in the cross section below the Coulomb barrier and the fact that the astrophysically relevant energies are particularly low, the measurement of the cross sections of charged-particles induced reactions is incredibly troublesome. For instance, during an experiment, which often involves cross sections in the range of pico to femto barn or lower, background radiation both from the cosmic rays and from the environment could become hugely problematic. In addition, the accelerator used in these experiments must possess two important characteristics: its potential must be stable over many hours in order to avoid changes in the measured yields and the energy spread of the beam must be the lowest possible.

Since the $^{12}\mathrm{C}(p,\gamma)^{13}\mathrm{N}$ measurement was performed at the LUNA experiment [28] in Italy, which is located under the Gran Sasso mountain, the cosmic background was drastically reduced. Furthermore, the LUNA 400kV accelerator, mounted in the underground laboratory, is able to provide a stable beam over many hours and with a particularly low energy spread (≤ 0.1 keV). These facts give an unique opportunity to obtain a very precise measurement of the reaction cross sections at exceptionally low energies.

In this chapter, I will provide some details about the background reduction at the LUNA experiment. Then, the experimental apparatus used in the $^{12}\mathrm{C}(p,\gamma)^{13}\mathrm{N}$ measurement will be thoroughly described. A specific section will be devoted to the targets that have beeen studied specifically in this thesis.

2.1 Background at the LUNA Experiment

The LUNA experiment is located in the underground laboratory at the Laboratori Nazionali del Gran Sasso (LNGS) in Italy, in the core of the Gran Sasso mountain. Considering that the minimum rock thickness is approximately 1400 m [29], the muon flux, originated from the interaction of the cosmic radiation with the upper atmosphere, is reduced by a factor of approximately 10^6 with respect to the one measured at the Earth's surface [30].

The cosmic background, in fact, is usually a significant source of background at $E_\gamma > 3$ MeV: high-energy charged particles from the outer space, mainly protons, interact with the nuclei in the atmosphere and produce showers of secondary radiation. At sea level it is mainly constituted by muons and electrons, the former being the most penetrating. Their interaction in the detector volume may be direct, producing ionization or bremsstrahlung by losing energy, or indirect, generating prompt or delayed radioactivity following the muon spallation on nuclei. The cosmic background reduction at LUNA is shown in Fig. 2.1, where the background spectrum taken on the surface is compared with the one obtained underground.

Hence, the only background detected by the γ-ray detector at LUNA, i.e. all the events that do not belong to the reaction of interest, is either due to the laboratory environment or is a beam-induced background. The latter is produced by the beam interaction with either the experimental setup materials or other impurities, and can be effectively removed by properly mantaining and cleaning the beam line elements. The laboratory background, instead, is produced by all the processes occurring in the environment where the setup is installed. The major contribution comes from the decay of radioisotopes occuring either in the mountain rocks, such as ^{40}K or the natural decay chains of ^{232}Th and ^{238}U, or in the air, such as ^{222}Rn. It can not be completely removed and accounts for the γ-ray lines at $E_\gamma < 3$ MeV. Nevertheless, this component of the background radiation can be significantly reduced by the use of the Pb shielding: its impact is clearly visible in Fig. 2.2, where the background events decrease by two orders of magnitude as a result of 15 cm thick Pb shield.

Finally, the environmental background at LUNA has been studied in several publications [31–33] which addressed many different aspects of diverse experimental setups used, and in each case, the presence of an unprecedented low environmental background was confirmed.

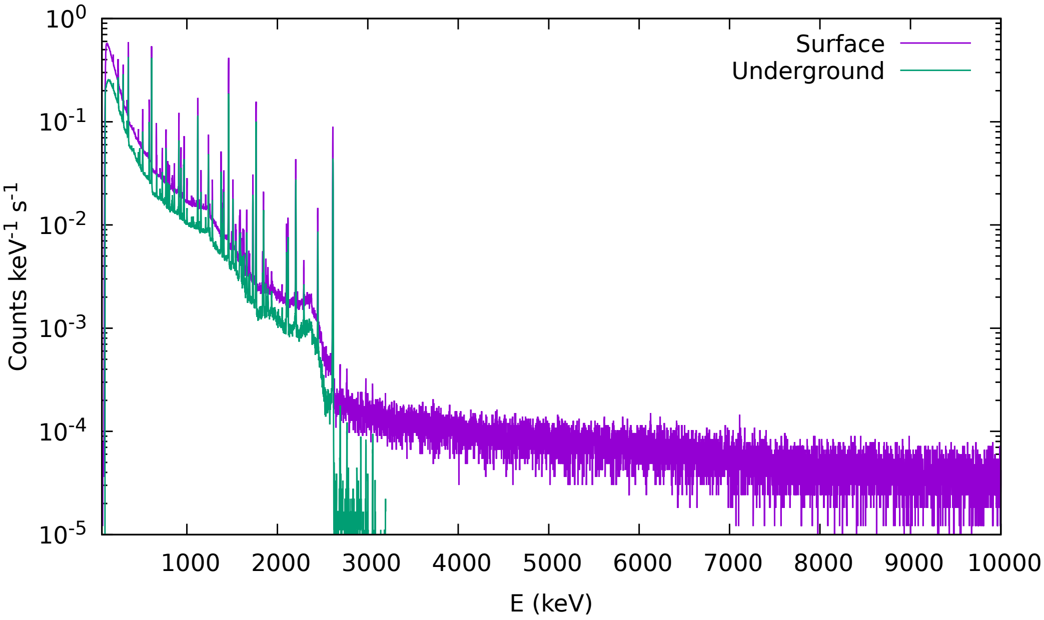

Figure 2.1: Comparison of two γ-spectra acquired with a HPGe detector on the Earth surface and at the LUNA laboratory. The background reduction is evident at $E_\gamma > 3$ MeV, as no muon background is detected underground.

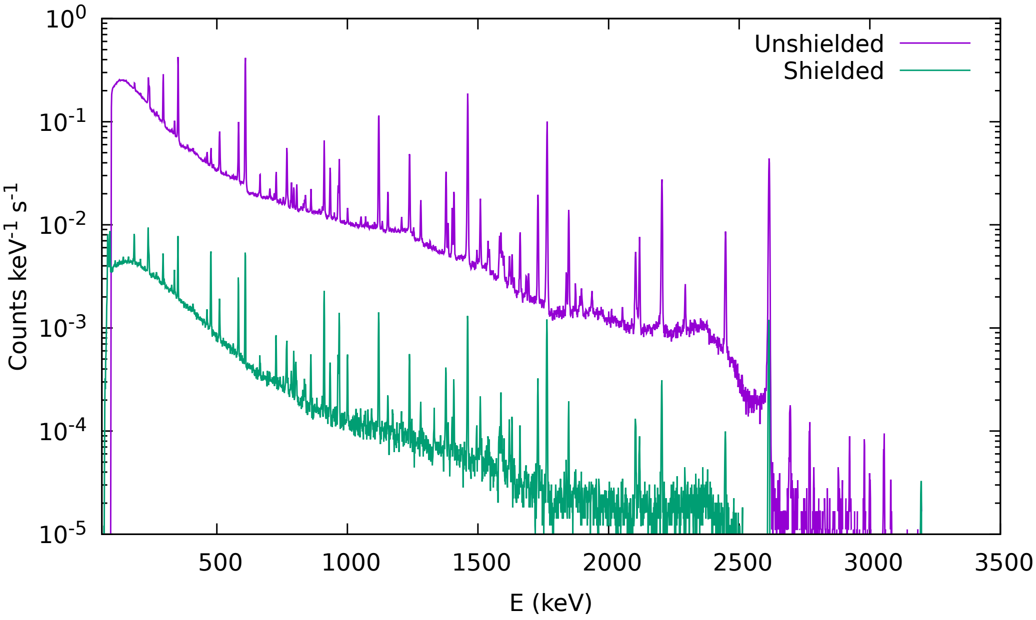

Figure 2.2: Comparison of two γ-spectra acquired with a HPGe detector at the LUNA facility. The background due to the environmental radioactivity is drastically reduced by the use of 15 cm thick Pb shielding.

2.2 Experimental Apparatus

2.2.1 LUNA Accelerator

The LUNA 400 kV electrostatic accelerator was built by High Voltage Engineering Europe, embedded in a tank which is filled with a gas mixture of N_2/CO_2 at the pressure of approximately 20 bar. The high voltage (HV) is generated by an Inline Cockcroft-Walton supply located inside the tank. The operating principle is the following: the capacitors are charged in parallel to a common potential, but then discharged in series. This prompt change between the series and parallel connections is accomplished by the use of rectifiers. As a result of this charging and discharging cycle, the terminal voltage is not constant, but has a small ripple that depends directly both on the external load resistance and on the period of the charging voltage. To prevent high electrical stress concentrations, it is important for all high voltage components to be electrically smooth. The equipotential rings on the accelerator tube, that can be seen in Fig. 2.3, and the large radii of corners and edges on the other components are necessary to reduce local electric stress and to prevent sparking.

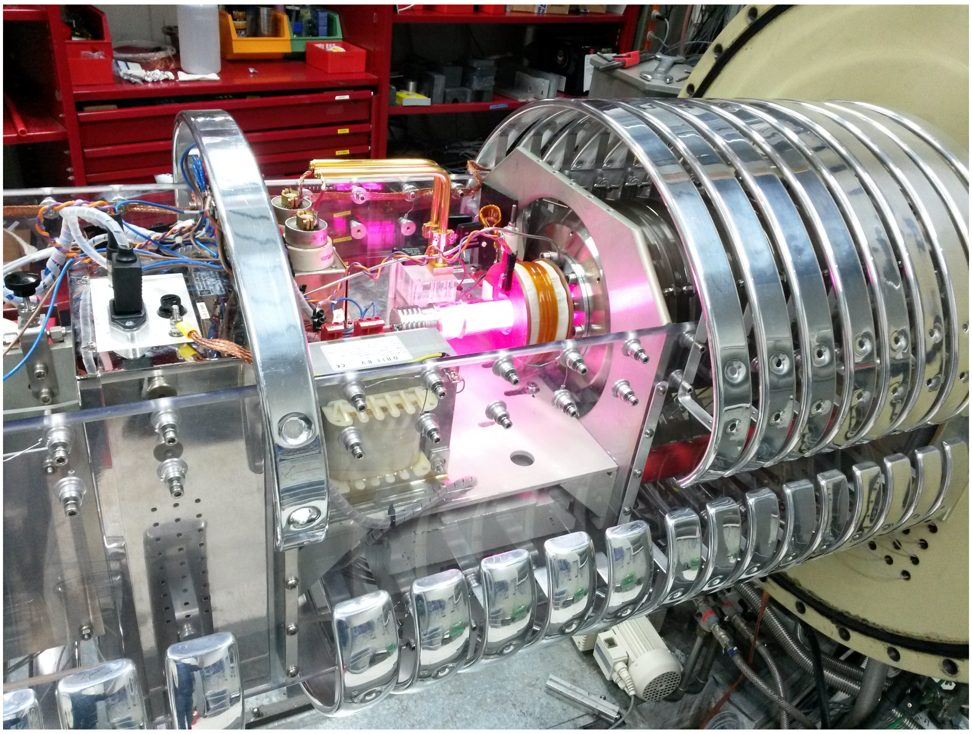

Figure 2.3: The RF source of the LUNA 400kV accelerator.

The source bottle contains a gas (hydrogen or helium) that is excited by Radio Frequency (RF) oscillator capacitively coupled to the bottle. The plasma is confined and positioned with an adjustable axial magnetic field. The ion source is mounted directly on the accelerator tube (Fig. 2.3). The source output is optimized by the control of the bottle pressure and oscillator loading. The ions are extracted by an electrode, which is part of the accelerator tube, and its voltage is thus included in the overall HV at the terminal. The accelerator tube is equipped with an adjustable shortening rod that permits a dynamical energy range from 50 kV to 400 kV, with an average beam current of $I = 500\ \mu A$, an energy spread of ±0.1 keV and stability of ±2 eV over $\sim$ 73 min [34].

2.2.2 Solid Target Beamline

Two different beamlines are installed on the LUNA 400kV: one costructed in order to study the reactions using a gas target, and the other used for the reactions on a solid target. Given the fact that the ^{12}C targets were solid, the latter line was used in the current experiment.

Once extracted from the source and accelerated, the proton beam is guided and focused to the target station using different stages of magnets and steerers. Immediately after the accelerator, a 45° magnet is used to provide the beam either to the solid target (0°) or to the gas target (45°) beamline. Focusing on the solid target one, a magnetic steerer is used in order to improve the beam trajectory. Another 45° magnet is located directly after: the 0° configuration ends with a Faraday cup; the 45° one, instead, drives the beam towards the target. At this point, several collimators and a steerer are positioned which are used to guide the beam towards the target chamber, and an another Faraday cup is present. Some of the collimators are used in order to provide the current measurements, useful to verify the beam trajectory and to focus it on the target. In addition, a turbo pump is installed in order to maintain a pressure of approximately 6×10^{-6} mbar inside the target chamber. Immediately prior to entering the target chamber the beam passes through a liquid nitrogen (LN_2) cooled copper tube that serves to to freeze out vaporous contaminants in the beamline vacuum. The tube is 1 m long and reaches few millimeters from the target. A bias voltage of - 300 V was applied to the copper tube to suppress secondary electrons emitted when protons strike the target. The scheme of a very similar apparatus, used for the previous campaign, can be seen in Fig. 2.4.

The ^{12}C targets used during the measurement were mounted on a target holder

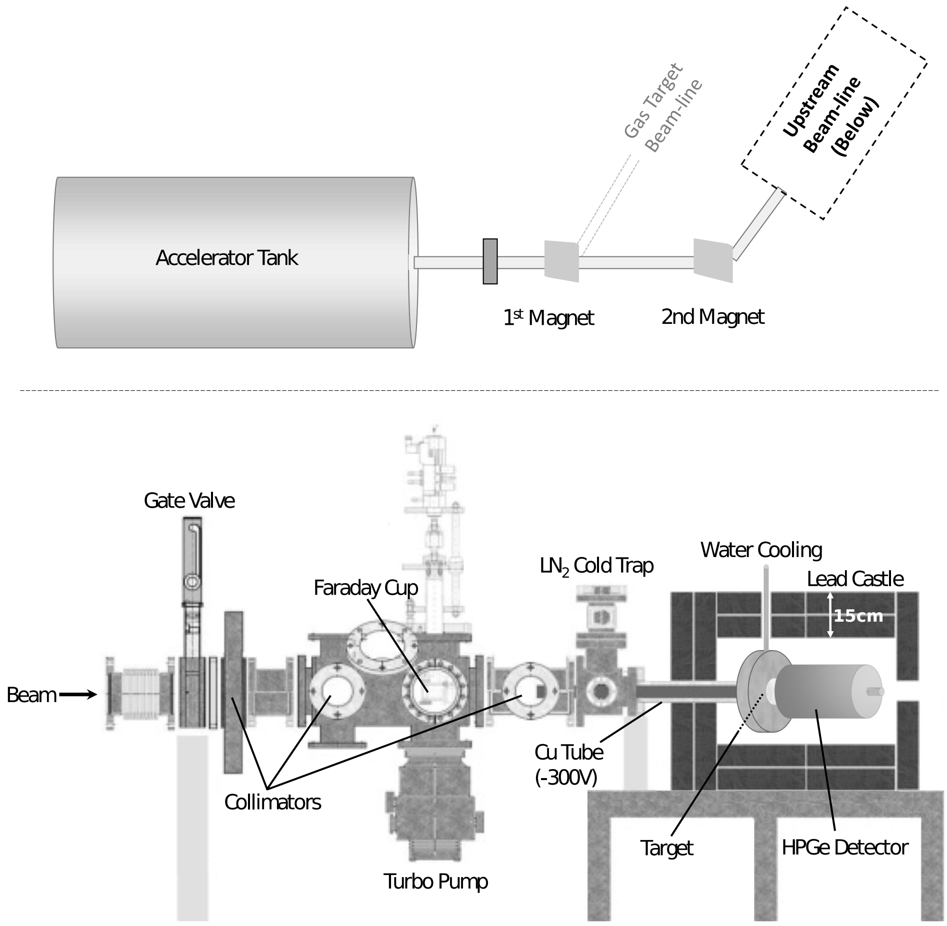

Figure 2.4: The scheme of the apparatus during the ^{17}O$(p,\gamma)^{18}$F measurement [35]. Upper: Sketch of the 400kV LUNA accelerator. Bottom: Sketch of the upstream portion of the solid target beamline.

positioned at 0° with respect to the beam axis. Deionized water was circulated in order to cool the targets and avoid any damage due to beam-heating effects. The target holder and the scattering chamber were electrically isolated from all the other beamline components and used as a Faraday cup. It allowed the determination of the total charge accumulated on the target over the course of irradiation. They were connected to the Digital Current Integrator module located in the control room.

An Ortec High Purity Germanium (HPGe) detector with relative efficiency of 104% [36] was positioned at 0° relative to the beam axis, at a distance of approximately 1.35 cm from the target surface. The detector and the attached integrated electro-mechanical cooling system were mounted on rails to provide an easy access to the target chamber. In order to reduce the background from the natural radioactivity, the entire target chamber and the detector were surrounded by a lead castle approximately 15 cm thick (see Fig. 2.2).

2.2.3 Electronic Chain

The two identical signal outputs from the HPGe detector preamplifier was attached to two amplifier modules (ORTEC 672), set at different settings in order to obtain two spectra with different gains. The purpose of the low gain channel, allowing the detection of high energy gamma-rays, was to observe the radiation originated from the presence of possible contaminants. The high gain channel was used for the data analysis as it results in larger number of channels per peak. The two were then connected to the Multichannel Analyzer (ORTEC ASPEC 927), connected through USB to the PC located in the control room. The MAESTRO software was used in order to acquire the spectra from the MCA.

The BNC PB-5 pulse generator was used for the dead time measurement. It was connected to the test input of the HPGe preamplifier, in order to obtain the pulser signal directly from the acquired spectra. In addition, the TRG OUT output of the pulser was connected both to the MCA counter and to the NIM counter (CAEN N1145) in the control room. This provided a useful cross-check of the pulser signal between the hardware and the software values.

Finally, the HVEE current integrator, located in the control room, was used in order to measure the charge accumulated on the target during each acquisition run. It was connected both to the control room NIM counter and to the MCA counter, as in the pulser case. The scheme for the full chain can be seen in Fig. 2.5.

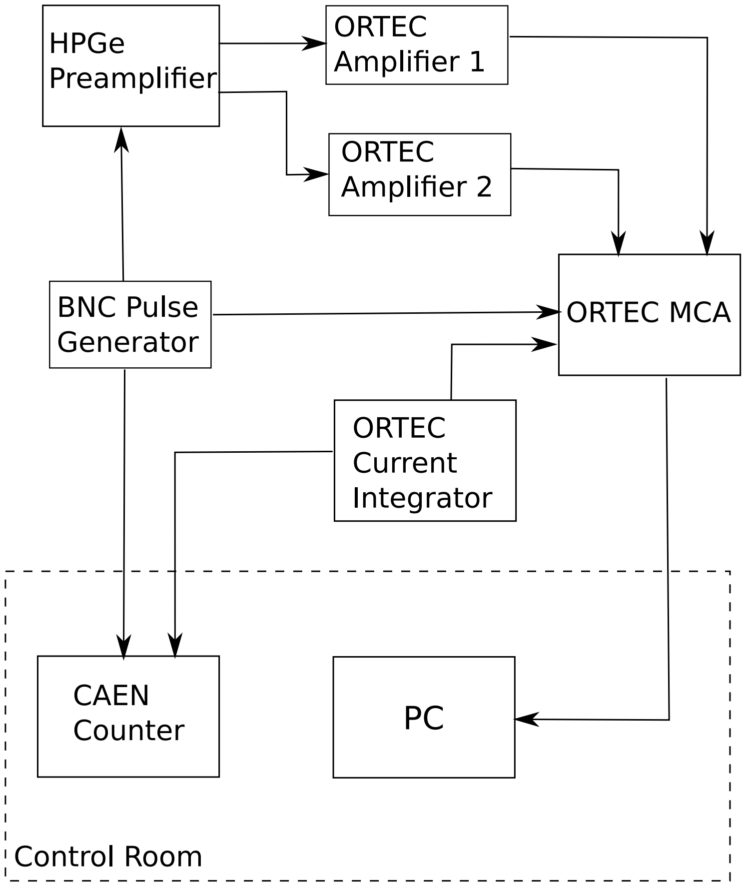

Figure 2.5: Scheme of the electronic chain used during the data acquisition.

2.3 Data Taking and Targets

The data obtained for the present study of the ^{12}C$(p, \gamma)^{13}$N reaction were acquired following a careful experimental procedure. After the target was mounted on the target holder, the beam was focused on the target and the data for the first, so-called, reference runs were taken. These runs, carefully performed each time at the same beam energy, were necessary in order to observe the target degradation. In addition, they were performed at two different detector positions, 0 cm and 15 cm. To each of these distances it is necessary to add 1.35 cm, corresponding to the actual distance between the target and the HPGe detector as the nominal position of 0 cm. Then, data were acquired at various beam energies until 15-20 C of charge had been accumulated on the target, and thus reference runs were repeated, usually once per day or more.

The monitoring of the targets through the use of reference runs is crucial as their degradation has an important effect on the observed γ-ray yield. In fact, the target thickness is necessary for the S-factor calculation. This will be more thoroughly discussed in Chapter 3. The list of all the runs for the thin targets can be seen in Tab. 2.2. The nominal thicknesses for the thin targets were obtained from the quartz oscillator at the moment of the target production, and does not correspond to the real thickness. On the contrary, the thickness of the *graphite* target was measured to be 6.7 mm thick directly in the laboratory.

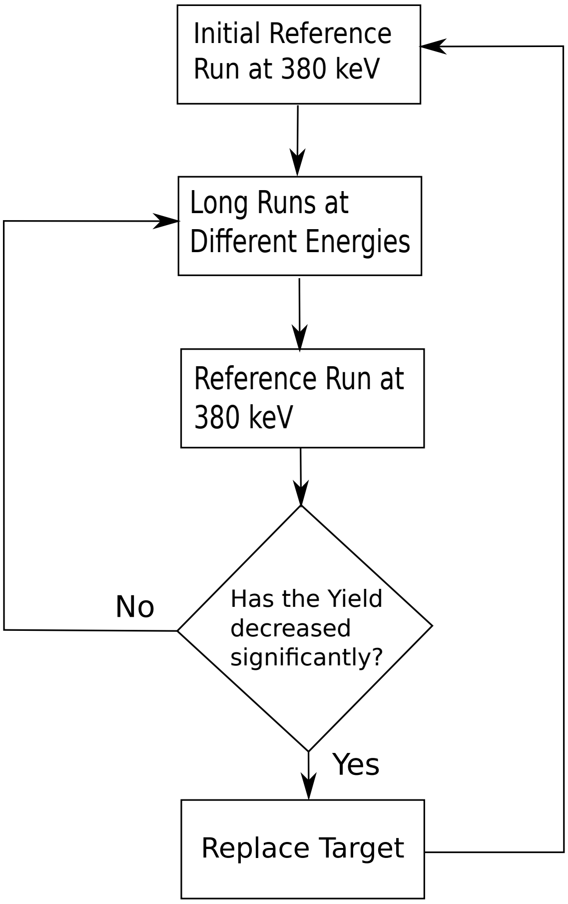

Figure 2.6: Flow chart depicting the procedure followed during the data acquistion for the thin ^{12}C targets.

This cycle of long measurements (typically performed over many hours, especially in case of low energies) of the $^{12}C(p,\gamma)^{13}N$ reaction alternated with reference runs was continued until the yield obtained from the γ-ray peak was approximately 40% lower than that observed on fresh target in reference run. The lead shield was then opened and a new target installed. The detector was carefully repositioned, the lead shield closed, and a new measurement started. In Fig. 2.6 provides a schematic representation of the procedure undertaken during the data acquisition.

All the targets used in this study are listed in Tab. 2.1. The main targets used for the measurements are the thin ones: the thick graphite target was used only as a test and only few runs were performed with it. The thin ^{12}C targets were produced at ATOMKI by the evaporation of natural carbon powder onto Ta backings: essentially, it consisted in heating up the material to evaporate in a vacuum chamber. This method allowed the creation of targets that can withstand long irradiation [37]. In addition, the target is expected to present the ^{13}C component of $\sim 1\%$, which must be taken into account during the analysis. In Fig. 2.7, a picture of the *nat*3 target mounted on the target holder is shown.

Name	Nominal Thickness	Accumulated Charge
nat3	~ 200 Å	~ 81.4 C
nat4	~ 200 Å	~ 67.6 C
nat8	~ 200 Å	~ 49.7 C
graphite	~ 6.4 mm	~ 10 C

Table 2.1: List of all the targets used in this study with their initial thicknesses and the total accumulated charge during the experiment.

Figure 2.7: Picture showing the fresh *nat3* target mounted on the target holder. The beamspot is visible in the middle of the target.

Run Number *(nat3)*	E_p keV	d cm	Q_{acc} C	Ref
129	378.7	1.35	0	x
130	378.7	16.35	0.06	x
131	378.7	1.35	0.08	x
132	158.4	1.35	0.36	
133	378.9	1.35	22.5	x
134	378.9	16.35	22.6	x
135	299.5	1.35	22.8	
136	319.4	1.35	23.1	
137	339.3	1.35	23.4	
138	359.2	1.35	23.6	
139	181.4	1.35	23.8	
140	151.6	1.35	25.5	
141	378.6	1.35	48.6	x
142	378.6	16.35	48.7	x
143	310.2	1.35	49.0	
145	280.4	1.35	49.5	
146	260.9	1.35	50.3	
147	171.7	1.35	51.0	
148	221.0	1.35	55.6	
149	241.1	1.35	57.2	
150	141.8	1.35	58.1	
151	378.6	1.35	81.2	x
152	378.6	16.35	81.4	x

Run Number *(nat4)*	E_p keV	d cm	Q_{acc} C	Ref
153	378.6	1.35	0	x
154	378.6	16.35	0.27	x
155	300.2	1.35	0.56	
156	100.1	1.35	0.95	
157	378.6	1.35	21.6	x
158	378.6	16.35	21.7	x
159	251.5	1.35	22.1	
160	110.7	1.35	22.9	
161	378.6	1.35	43.0	x
162	378.6	16.35	43.1	x
163	290.2	1.35	43.5	
164	290.8	1.35	43.8	
165	190.2	1.35	44.2	
166	230.3	1.35	48.8	
167	329.8	1.35	50.1	
168	120.1	1.35	50.3	
169	378.6	1.35	67.5	x
170	378.6	16.35	67.6	x

Run Number *(nat8)*	E_p keV	d cm	Q_{acc} C	Ref
200	377.4	16.35	0	x
201	377.4	1.35	0.23	x
202	89.8	1.35	0.28	
203	379.4	1.35	14.0	x
204	379.4	16.35	14.1	x
205	89.7	1.35	14.4	
206	379.4	1.35	32.8	x
207	379.4	16.35	32.9	x
208	379.4	1.35	33.1	x
209	89.7	1.35	33.2	
210	379.3	1.35	49.6	x
211	379.4	16.35	49.7	x

Run Number *(graphite)*	E_p kev	d cm	Q_{acc} C
348	380.0	1.75	0.11
349	380.0	1.75	0.12
350	380.0	1.75	0.14
351	380.0	1.75	0.15
352	380.0	1.75	0.18
353	380.0	1.75	0.23
354	380.0	1.75	0.29
355	380.0	1.75	0.39
356	380.0	1.75	0.41
357	200.6	1.75	0.86
358	200.6	1.75	0.87

Table 2.2: List of the runs for all the targets: E_p is the beam energy, d is the detector distance at which the run was performed and Q_{acc} is the total accumulated charge on the target at the beginning of each run. The last column indicates if the run was a reference one.

Chapter 3

Data Analysis

In this chapter, I will discuss the data analysis procedure and present the results from the current study of the $^{12}\mathrm{C}(p,\gamma)^{13}\mathrm{N}$ reaction. Firstly, I will introduce the notions of yield and stopping power. Then I will explain the method used for the detector efficiency determination. Next, I will talk about the Peak Shape Analysis, performed in order to obtain information about the target degradation. Finally, I will present the observed yields of the prompt γ-rays, and I will attempt the extraction of the S-factor.

3.1 Yield and Cross Section

In order to experimentally obtain the absolute cross section of a nuclear reaction, it is necessary to identify the reaction products. In the case of the $^{12}\mathrm{C}(p,\gamma)^{13}\mathrm{N}$ reaction, this involves measuring the intensity of the emitted γ-rays.

The *reaction yield* is defined as the ratio of the total number of reactions, N_R, and the total number of incident beam particles, N_b. Thus, experimentally speaking, the total yield is given by:

$$Y = \frac{N_\mathrm{R}}{N_\mathrm{b}} = \frac{N_\gamma}{N_p \eta_{ph}(E_\gamma) W(\theta) Br} \tag{3.1}$$

where N_γ is the number of observed gamma rays, N_p is the number of incoming protons, Br is the branching ratio of the γ-ray transition, $\eta_{ph}(E_\gamma)$ is the detector efficiency and $W(\theta)$ is the angular distribution factor . In case of the $^{12}\mathrm{C}(p,\gamma)^{13}\mathrm{N}$ at

LUNA, the reaction proceeds only to the ground state, thus $Br = 1$. Furthermore, the angular distribution of the γ-ray is assumed to be isotropic, thus also $W(\theta) = 1$.

The total yield can also be expressed in terms of the reaction cross section, σ, and the number of target nuclei available through the target thickness [9]:

$$Y = \frac{N_{\mathrm{R}}}{N_{\mathrm{b}}} = \int_{E_0-\Delta E}^{E_0} \frac{\sigma(E)}{\epsilon_{\mathrm{eff}}(E)} dE \tag{3.2}$$

where $\epsilon_{\mathrm{eff}}(E)$ is the effective stopping power and accounts for the number of nuclei per unit area available in the target, ΔE is the total energy lost by the beam after interacting with the target and E_0 is the beam energy (next sections provides a complete discussion of these quantities).

In case of the $^{12}\mathrm{C}(p,\gamma)^{13}\mathrm{N}$ non-resonant component, it is possible to use the Equation 1.14 to rewrite the Equation 3.2:

$$Y = S(E_{\mathrm{eff}}) \int_{E_0-\Delta E}^{E_0} \frac{1}{\epsilon(E)E} e^{-2\pi\eta(E)} dE \tag{3.3}$$

where the S-factor was assumed to be constant over the target thickness.

The S-factor is associated to the *effective energy*, E_{eff}, which is defined as the weighted average of the energy over the target thickness:

$$E_{\mathrm{eff}} = \frac{\int_{E_0-\Delta E}^{E_0} E\sigma(E)dE}{\int_{E_0-\Delta E}^{E_0} \sigma(E)dE} \tag{3.4}$$

Hence, combining Equation 3.1 and 3.3 it is possible to extract the information about the reaction S-factor by obtaining experimentally the total yield measurement. Nevertheless, in order to achieve it, it is first necessary to gain insight about the detector efficiency, $\eta_{\mathrm{ph}}(E_\gamma)$, the target thickness, ΔE, and the stopping power, $\epsilon(E)$. The derivation of these quantities will be discussed in the following sections.

3.1.1 Stopping Power

A charged particle that passes through a certain material slows down losing a part of its energy primarily due to the inelastic collisions with atomic electrons. The rate of energy loss is referred to as *linear stopping power*, $\epsilon_{\text{lin}}(E)$:

$$\epsilon_{\text{lin}}(E) = -\frac{dE}{dx} \tag{3.5}$$

where dE is the infinitesimal energy loss in the infinitesimal spatial distance dx.

The stopping power is commonly expressed in terms of the energy loss per unit areal density, ρ (typically given in units of atoms per cm^2):

$$\epsilon(E) = -\frac{1}{N}\frac{dE}{dx} \tag{3.6}$$

where N is the number density (atoms per cm^3) of the target material.

The theoretical treatment of the interaction of charged particles in the matter is rather complex. However, the Bethe formula [38] provides fairly good prediction of the energy lost by a charged particle when passing through matter at high projectile energies:

$$-\frac{dE}{dx} = \frac{4\pi e^4 z^2}{m_e v^2} NB \tag{3.7}$$

where

$$B \equiv Z\left[\ln\left(\frac{2m_e v^2}{I}\right) - \ln\left(1 - \frac{v^2}{c^2}\right) - \frac{v^2}{c^2}\right] \tag{3.8}$$

This equation describes the theoretical stopping power for a projectile of charge z, and velocity v, passing through a medium composed of atoms of atomic number Z. The ionization potential is represented by I, and m_e is the electron mass. The most important information that is provided by this description is the fact that the stopping power is inversely propotional to the energy (as $E \propto v^2$), and the fact that the energy loss is directly proportional to the charge of both projectile and target.

The discussion, so far, was limited to targets composed by purely one element. Obviously, in nuclear physics experiments that is often not the case. Usually, the target is made of several different elements. Moreover, the presence of contaminants must be taken into account. In this case a quantity known as the *effective stopping power*, ϵ_{eff}, must be calculated [3]:

$$\epsilon_{\text{eff}} = \epsilon_a + \sum_i \frac{N_i}{N_a}\epsilon_i \tag{3.9}$$

where the relevant target nuclei, N_a, are referred to as *active* and N_i are the *inactive* nuclei present in the target, that do not take part in the reaction, but nevertheless take part in the slowing down of the projectile.

In the case of ^{12}C targets used in the present experiment, the effective stopping power is given by:

$$\epsilon_{\text{eff}}(^{12}\text{C}) = \epsilon(^{12}\text{C}) + \frac{N(^{13}\text{C})}{N(^{12}\text{C})}\epsilon(^{13}\text{C}) \tag{3.10}$$

where the presence of a fraction of ^{13}C nuclei is considered. Since the stopping power of the C isotopes is approximately the same, it is possible to simplify the formula as follows:

$$\epsilon_{\text{eff}}(^{12}\text{C}) = \frac{N(\text{C})}{N(^{12}\text{C})}\epsilon(\text{C}) \tag{3.11}$$

The computer code SRIM [39] provides the proton stopping power tables for different materials, required for the $^{12}\text{C}(p,\gamma)^{13}\text{N}$ analysis with an uncertainty of 6.4% [40]. These are based both on experimental measurements and theoretical predictions. In the Fig. 3.1 the stopping powers for the ^{12}C nuclei is illustrated as a function of proton energy.

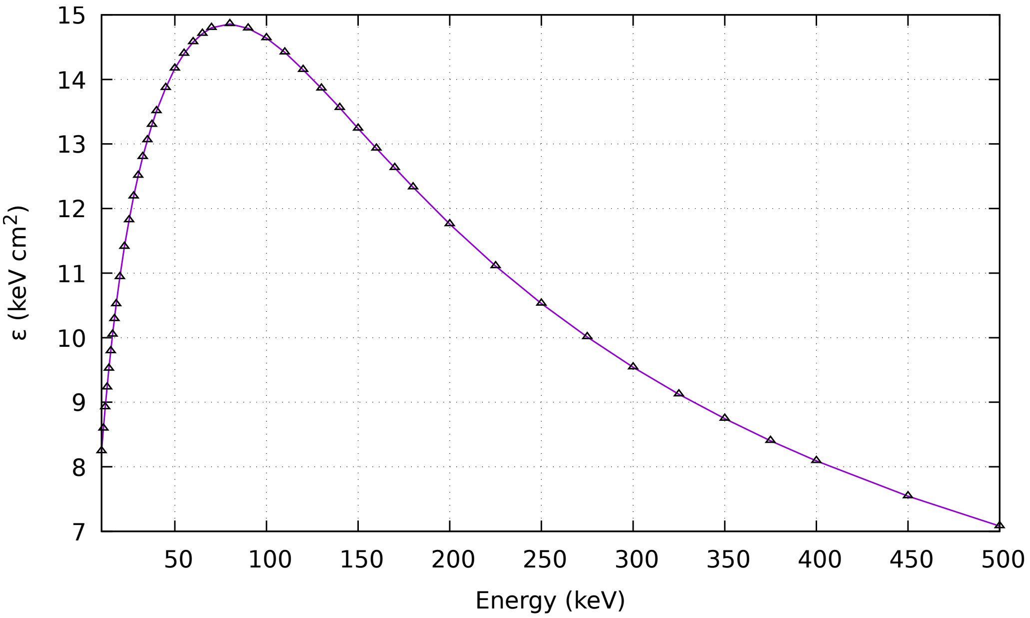

Figure 3.1: SRIM stopping power for protons inside the carbon target.

3.2 Calibration

The HPGe detector used in this study was calibrated with the γ-rays from ^{137}Cs, ^{60}Co and ^{88}Y calibration sources. The data for the calibration sources used during the experiment are given in Tab. 3.1.

Source	Activity	γ-rays	Branching
^{60}Co	0.266(4) kBq 5.79(5) kBq	1173.228(3) keV 1332.492(4) keV	0.9985(3) 0.999 826(6)
^{137}Cs	2.80(4) kBq	661.659(3) keV	1
^{88}Y	23.7(1) Bq	898.05(1) keV 1836.090(8) keV	0.937(3) 0.9939(3)

Table 3.1: Data for the calibration sources used during the experiment. Two different activities at the acquisition time are listed for the ^{60}Co as two different sources were used.

Since two different acquisition channels were used, two different calibration curves had to be determined. Linear fits (Fig. 3.2) were performed in order to determine the following relationship between γ-ray energy and spectrum channel number:

$$E_\gamma = a + b \times \text{Channel} \tag{3.12}$$

The obtained parameters can be seen in Tab. 3.2. The calibration was tested at different times during the data acquistion and was found to remain constant.

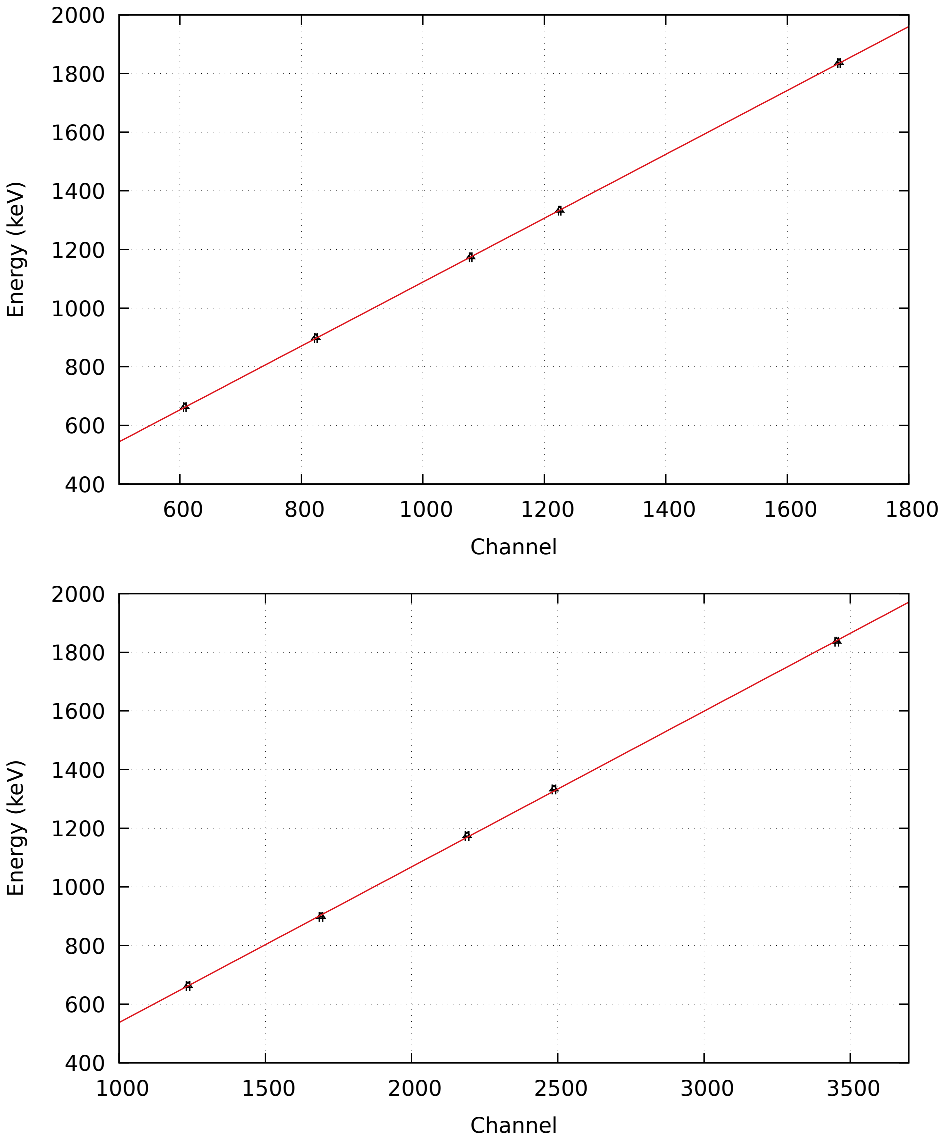

Figure 3.2: HPGe detector energy calibration fit for both *Ch1* (upper) and *Ch2* (lower).

Acq. Channel	a	b	χ^2/dof
1	0(2)	1.089(2)	0.54
2	6(8)	0.531(3)	0.93

Table 3.2: Fit parameters for the HPGe detector calibration. Results for both *Ch1* and *Ch2* are shown.

3.3 Efficiency

The detection efficiency of the experimental setup was determined by using two calibration sources, ^{137}Cs and ^{60}Co, and the γ-rays of the ^{14}N$(p,\gamma)^{15}$O resonance at $E_p = 278$ keV. The ^{88}Y source was not used in this case as its statistics was very low at distances higher than 1.65 cm from the detector. In fact, its activity at measurement time was ~ 24 Bq.

The γ-rays of the ^{14}N(p,γ) resonance range from 0.7 MeV to 7.6 MeV, giving an opportunity to check the detector response in a very wide range of energies. In this case, three distinct γ-cascades are used, in which each secondary state decays exclusively to the ground state. The ^{15}O level scheme can be seen in Fig. 3.3. The associated spectrum acquired at LUNA can be seen in Fig. 3.4. The calibration sources (see Tab. 3.1), instead, were used in order to fix the energy efficiency in the range up to 1.3 MeV. The ^{137}Cs present a single γ-ray at 662 keV. The ^{60}Co, instead, emits two different γ-rays in cascade: the primary at 1173 keV, and the secondary at 1332 keV.

In a nuclear physics experiment, the efficiency is usually calculated using the calibration sources activities, A. The absolute full-energy peak efficiency is, indeed, defined as the ratio between the measured peak area and the number of γ-rays emitted at the same energy in the whole solid angle by a radioactive nuclide. It can be determined as:

$$\eta_{ph} = \frac{N_{\text{counts}}}{A \Delta t Br} \tag{3.13}$$

where N_{counts} is the number of counts inside the γ-peak of interest, Δt is the acquisition time and Br is the branching ratio of the emitted γ-ray. Even though this approach works flawlessly in the case of ^{137}Cs source, it does not apply well for the ^{60}Co and the ^{14}N resonance.

When a detector is in close geometry with respect to the γ-source, the efficiency calculation is, in fact, made problematic by the presence of the *true-coincidence*

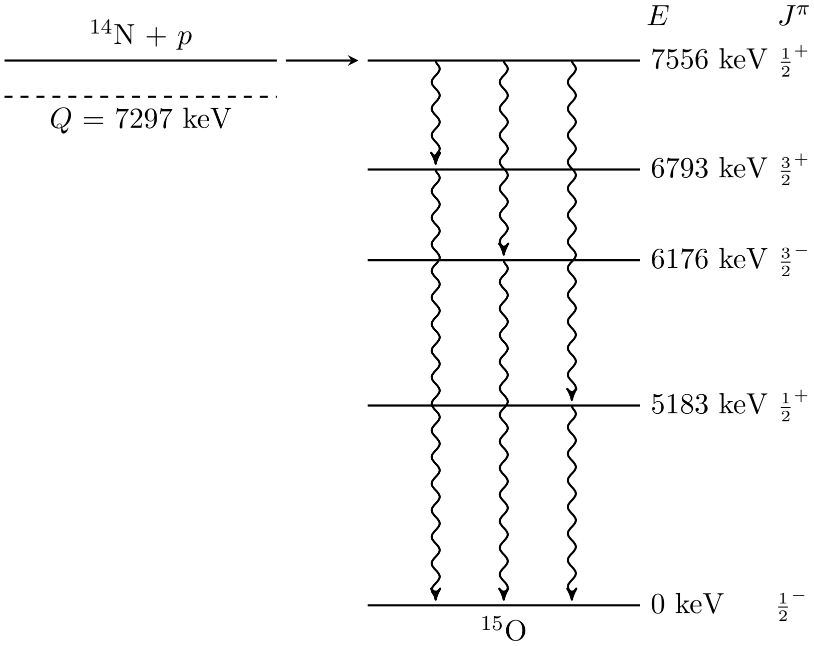

Figure 3.3: The level scheme of the ^{14}N$(p,\gamma)^{15}$O reaction. Three different decay cascades are used for the detection efficiency determination.

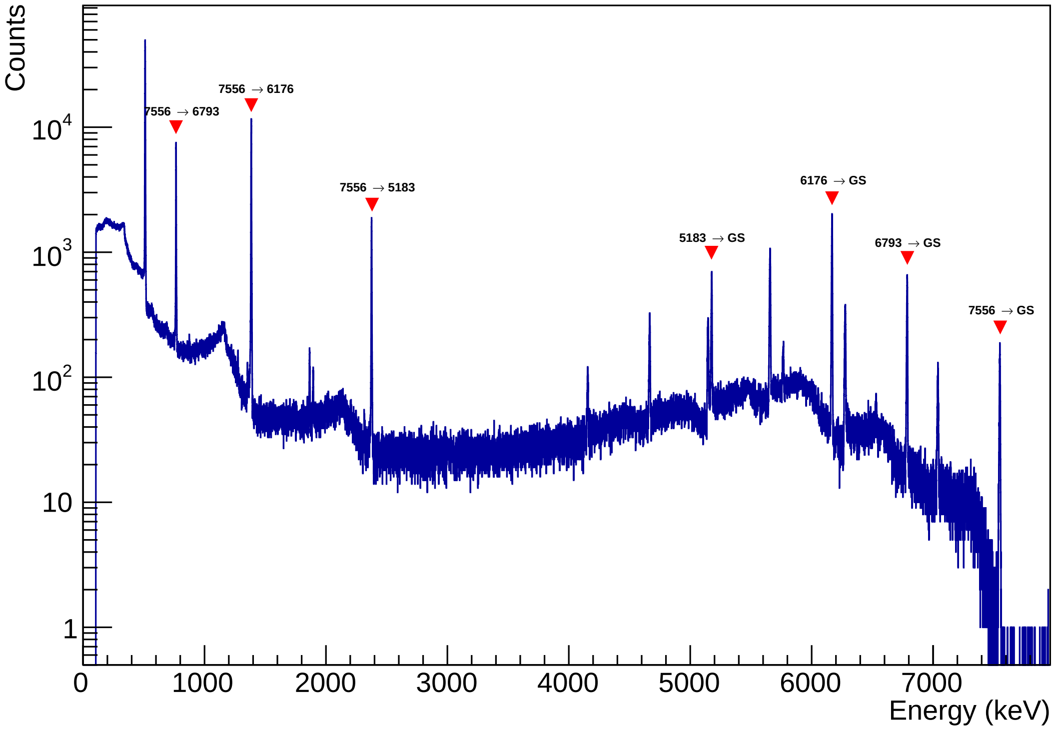

Figure 3.4: Spectrum of the ^{14}N resonance at $E_p = 278$ keV.

summing [41]. The typical lifetime of intermediate excited states in the decay of ^{60}Co and in ^{14}N(p,γ) is usually in the range of picoseconds or lower. The typical response time for a HPGe detector, i.e. the minimum time between two photon events that is needed for the detector to recognize these as two separate events, is in the order of microseconds. This is several orders of magnitude longer than the typical lifetime of the excited states. For decays where two or more photons are emitted in cascade there is a significant probability that multiple photons will interact with and deposit energy in the detector. Since the time between the photon emissions is much shorter than the response time of the detector, it is not possible for the detector to distinguish the photons as separate events and only one pulse is generated, which corresponds to the sum of the individual deposited energies. Because of this, two different effects arise:

- One of the photons might deposit all of its energy in the detector and the other photon might deposit some or all of its energy in the detector. This will move a count from the full-energy peak of the first photon to a higher energy in the spectrum. This reduces the count rate of the first photon compared to the detection of only a single photon. This phenomenon is called *summing-out* and can be seen in Fig. 3.5 for the ^{60}Co case.
- Both photons might deposit all of their energies in the detector. Fig. 3.5 shows ^{60}Co spectra taken with the detector both in close geometry (1.35 cm from the source) and far geometry (16.35 cm from the source). It can be seen how the transition at 2505 keV, which has a branching of 2×10^{-6}, is enhanced. This effect is called *summing-in.*

In case of the efficiency calibration, the peaks affected by the summing-in are not considered, thus only the summing-out must be taken into account. The result of this effect is that the efficiencies, that could have been calculated from the nominal activities of the calibration sources, using Equation 3.13, will appear to be lower than the true efficiency of the detector. If these peaks are used without correction, then the calculated efficiency will be shifted towards lower values.

Furthermore, the probability of true-coincidence summing is dependent on the detection geometry: the effect, in fact, can be reduced by moving the sample away from the detector. For this reason, the measurements both of the radiactive sources and of the ^{14}N(p,γ) resonance were performed at four different distances, d, between the source and front face of the detector: 1.35 cm, 6.35 cm, 11.35 cm and 16.35 cm. In close geometry the effects of summing-out were as high as 21%,

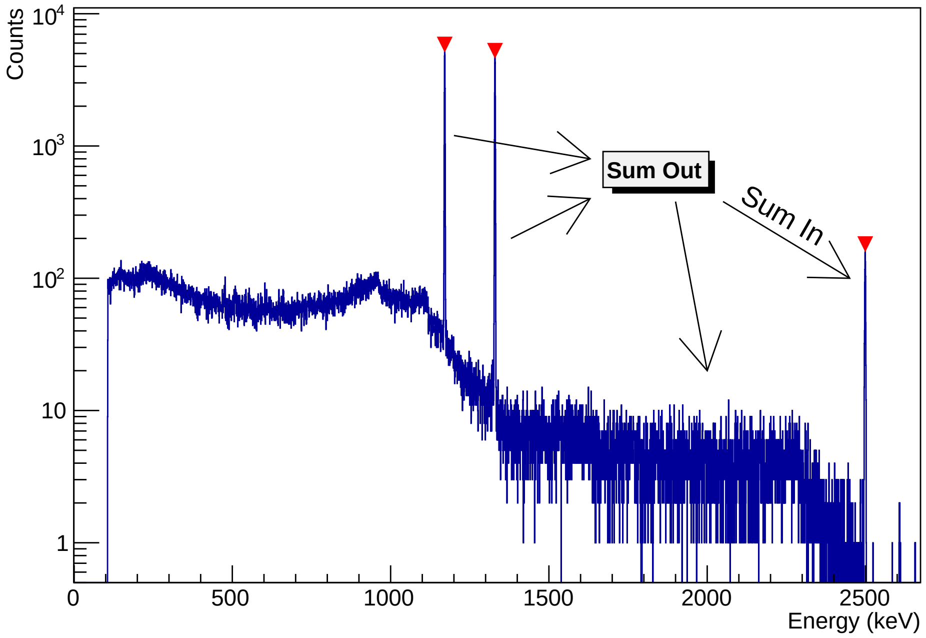

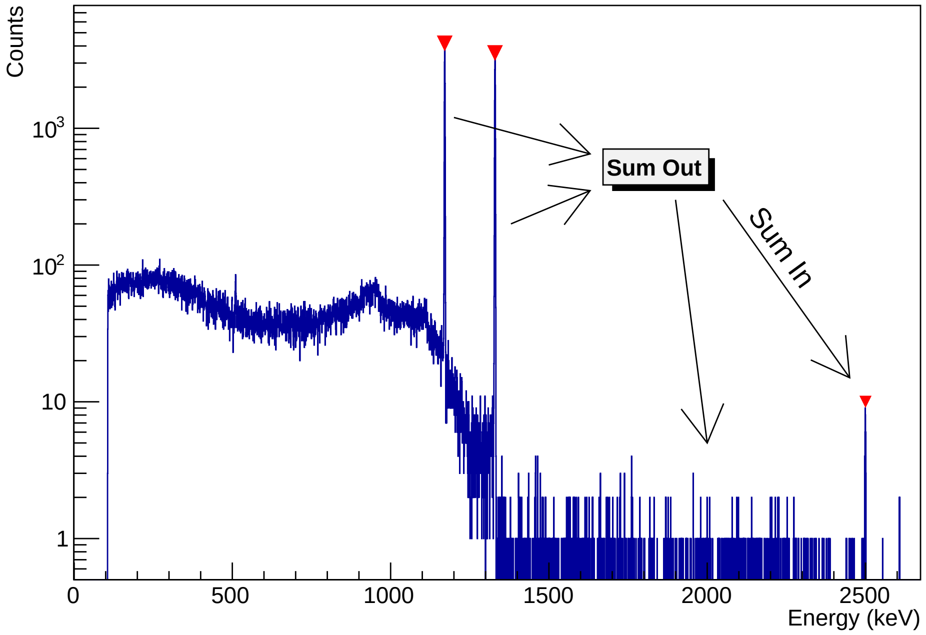

Figure 3.5: Two spectra of the ^{60}Co calibration source. Some events of the γ-rays at the 1173 keV and 1332 keV are seen in coincidence by the detector and create both the sum peak at 2505 keV and the events in between. The upper spectrum was taken at $d = 1.35$ cm. The lower spectrum was taken at $d = 16.35$ cm. In the latter, the summing is much lower due to higher distance from the detector.

while corrections of less than 3% were necessary for the measurements performed at $d = 16.35$ cm.

In order to take into account the problem of the summing-out effect, the following procedure was followed for the efficiency estimation [42]:

- The photopeak efficiency and the total efficiency were parametrized as:

$$\eta_{ph}(d, E_\gamma) = D \exp[a + b\ln(E_\gamma) + c\ln^2(E_\gamma)] \tag{3.14}$$

$$\ln\left(\frac{\eta_{ph}}{\eta_{tot}}\right) = k_1 + k_2\ln(E_\gamma) + k_3\ln^2(E_\gamma) \tag{3.15}$$

  where a, b, c, k_1, k_2 and k_3 are free parameters, and D is a function of distance that includes the detector dimensions:

$$D = \frac{1 - \exp\left(-\frac{d+d_0}{d_1+d_2\sqrt{E_\gamma}}\right)}{(d+d_0)^2} \tag{3.16}$$

  where d_0, d_1 and d_2 are free parameters that define the detector geometry.

- The *observed* yields of the peaks were calculated using the following:

$$Y_{\gamma,i} = \frac{N_{\gamma,i}}{t} \tag{3.17}$$

  where $N_{\gamma,i}$ is the number of counts inside the peak of either the primary or the secondary γ-ray, and t is the total time of the data acquisition. Hence, it was possible to parametrize the observed yields as:

$$Y_{\gamma,1} = Rb_i\eta_{ph}(E_{\gamma,1})(1 - \eta_{tot}(E_{\gamma,2})) \tag{3.18}$$

$$Y_{\gamma,2} = Rb_i\eta_{ph}(E_{\gamma,2})(1 - \eta_{tot}(E_{\gamma,1})) \tag{3.19}$$

  where b_i is the branching of the primary γ-ray and R is either the activity of the calibration source, or, in case of a resonance, a free parameter. In this way, the summing-out effect is taken into account: in fact, the $\eta_{ph}(E_{\gamma,1})$ term can be interpreted as the probability that the detector sees the primary γ-ray, and the product $\eta_{ph}(E_{\gamma,1})\eta_{tot}(E_{\gamma,2})$ is the combined probability that the primary is detected as the full-energy peak and the secondary one will be seen anywhere in the spectrum. In addition, these equation assume isotropic angular distributions and correlations of the γ-rays.

- Each $^{14}\mathrm{N}(p,\gamma)^{15}\mathrm{O}$ γ-cascade was chosen such that the secondary excited state, that is fed by the primary one, then decays to the ground state with $\sim$ 100% probability. This allows to set constraints on the efficiency curve arising from the one-by-one equality of the intensities of primary and secondary transitions involving each excited state:

$$\frac{Y_{\gamma,1}}{Y_{\gamma,2}} = \frac{\eta_{ph}(E_{\gamma,1})(1-\eta_{tot}(E_{\gamma,2}))}{\eta_{ph}(E_{\gamma,2})(1-\eta_{tot}(E_{\gamma,1}))} \tag{3.20}$$

- All these constraints were used in a global multiparametric chi-squared minimization, using the γ-ray yields recorded at all four distances (see [42] for a similar procedure). In order to perform the minimization, an algorithm from Hyperopt [43] library, based on Markov Chains, was utilized.

The resultant efficiency curve for $d = 1.35$ cm is shown in Fig. 3.6 alongside the observed efficiencies for the calibration sources. The optimal parameters are shown in Tab 3.3. As the $^{137}\mathrm{Cs}$ produces only one γ-ray, the summing effect is non existent, and for this reason, the curve was constrained to pass through that point. Since the calculation of the the efficiency uncertainty is non-trivial, given the high number of free parameters, for the scope of this thesis a conservative uncertainty of 5% on η_{ph} is assumed in the following. More rigorous derivation of the associated error must be performed in the future analysis at LUNA.

a	b	c	k_1	k_2	k_3	d_0 cm	d_1 cm	d_2 cm	R
0.085	-0.614	-0.077	-1.5	-0.355	-0.17	2.02	0.11	5.54	43

Table 3.3: Retrieved parameters for the efficiency parametrization.

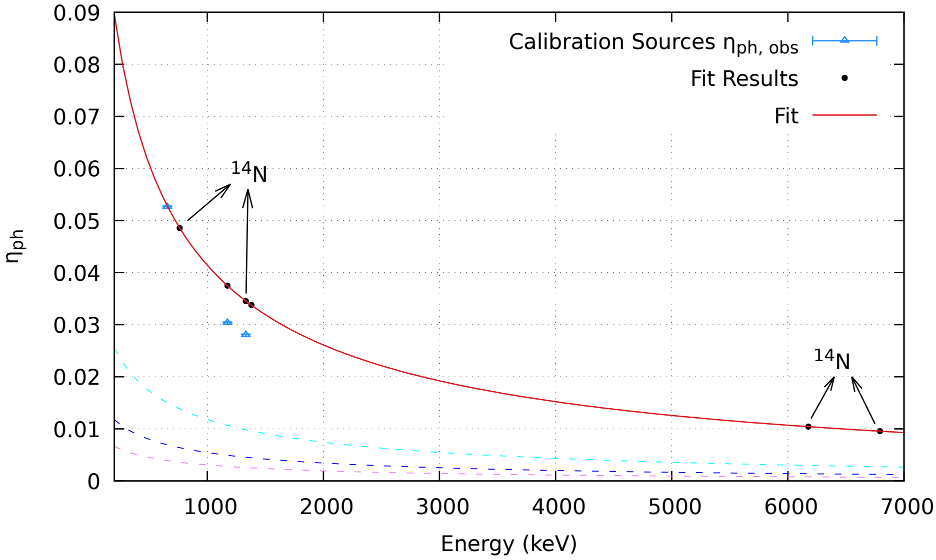

Figure 3.6: Efficiency curve obtained from the multiparametric fit ($d = 1.35$ cm). The observed efficiencies from the calibration sources were plotted in order to show the amplitude of the summing out correction. Dashed lines correspond to the efficiencies at higher distances: 6.35 cm (cyan), 11.35 cm (blue) and 16.35 cm (violet).

3.4 Peak Shape Analysis

As mentioned in the Section 2.3, different reference runs were performed for each target in order to monitor their degradation and to derive the ΔE. The beam energy during these runs was always set at approximately 380 keV (see Section 2.3), and they were done after a significant amount of charge was accumulated on the targets (approximately every 15 C). The $^{12}\text{C}(p,\gamma)^{13}\text{N}$ reaction peak from these runs can be used in order to extract information on the target thickness, necessary to obtain the S-factor of the reaction.

The shape of the γ-peak is, in fact, determined by the cross section, $\sigma(E_p)$, behaviour in the energy range spanned by the incident beam inside the target during the slowing down process. For an infinitesimal layer, dE, of the ^{12}C target, the corresponding infinitesimal reaction yield, dY, per incident particle can be written as:

$$dY = \frac{\sigma(E)}{\epsilon_{\text{eff}}(E)} dE \tag{3.21}$$

where $\epsilon_{\text{eff}}(E)$ is the effective stopping power of the beam inside the target, defined as in Equation 3.11.

It is possible to make a transformation from the energy E_p at which the reaction takes place to the corresponding γ-ray energy, E_γ, by using the following relationship:

$$E_\gamma = Q + \frac{M}{m+M}E_p - \Delta E_{\text{Rec}} + \Delta E_{\text{Dopp}} \tag{3.22}$$

where Q is the Q-value of the $^{12}\text{C}(p,\gamma)^{13}\text{N}$ reaction (1943.5(2) keV), M and m are respectively ^{12}C and proton masses, ΔE_{Rec} is the correction for the recoil effect of the ^{13}N compound nucleus and ΔE_{Dopp} is the correction for the Doppler effect. The last two terms are defined as:

$$\Delta E_{\text{Rec}} = \frac{E_\gamma^2}{2M_{^{13}\text{N}}c^2} \ (\sim 2 \text{ keV}) \tag{3.23}$$

$$\Delta E_{\text{Dopp}} = \frac{v}{c}E_\gamma \cos\theta \ (\sim 10 \text{ keV}) \tag{3.24}$$

where c is the speed of light, v is the compound nucleus velocity and θ is the angle between the beam direction and the γ-ray detector, which is assumed to be 0° given the current experimental setup. The estimates on the right were calculated assuming beam energies of 380 keV.

By differentiating the Equation 3.22:

$$dE_\gamma = \frac{M}{m+M}dE_p \tag{3.25}$$

where the correction terms are negligible.

Now by substituting this expression into Equation 3.21:

$$dY = \frac{\sigma(E_p)}{\epsilon_{\text{eff}}(E_p)}\frac{m+M}{M}dE_\gamma \tag{3.26}$$

The next step consists into replacing the infinitesimal values, dY and dE_γ, with those given by each bin of the acquired spectra, Y_i and $\Delta E_{\gamma,i}$, where i is the index attributed to each bin of the γ-peak. In order to do this, a precise energy calibration is needed for each run. The values from Section 3.2 were used. In addition, during the conversion from each $E_{\gamma,i}$ to the corresponding $E_{p,i}$, the correction for the Doppler and recoil effects must be considered. Furthermore, both the energy resolution and efficiency of the detector must be taken into account. Thus, the reaction yield of a single bin, Y_i, which corresponds to the energy range from $E_{\gamma,i}$

to $(E_{\gamma,i} + \Delta E_{\gamma,i})$, is given by the following expression:

$$Y_i = K\frac{\sigma(E_{p,i})}{\epsilon_{\text{eff}}(E_{p,i})}\eta_{ph}(E_{\gamma,i})F(E_{\gamma,i},\sigma_{\text{HPGe}}(E_{\gamma,i}))\Delta E_{\gamma,i} \tag{3.27}$$

where $F(E_{\gamma,i},\sigma_{\text{HPGe}}(E_{\gamma,i}))$ is the gaussian convolution term, which models the detector resolution for each bin, and K is a free parameter.

The yield of each bin, Y_i, is proportional to the cross section $\sigma(E_{p,i})$ associated to the proton energy $E_{p,i}$, which can be obtained by using Equation 3.22. All the other terms, in fact, do not contribute greatly as they vary rather slowly in the range of the target thickness. Hence, γ-ray peak shape associated with the transition is modulated by the energy dependence of the cross section as the beam loses energy passing through the target. This can be visualized in the Fig. 3.7. Hence, by studying the shape of the ^{12}C$(p,\gamma)^{13}$N γ-peak, the target thickness can be extracted.

In order to analyze the shape of the γ-peak, a parametrization of the target profile is needed. In fact, the peak width will depend not only on the target thickness, but also on its profile (i.e. the number of target nuclei as a function of the depth), which can change as the target is irradiated. This effect can be clearly observed in Fig. 3.8. The profile can be modelled as the product of two Fermi functions [44]:

$$P(E) = \left[\exp\left(\frac{E-E_0}{\Gamma_1}\right)+1\right]^{-1}\left[\exp\left(\frac{E_0-E-\Delta E}{\Gamma_2}\right)+1\right]^{-1} \tag{3.28}$$

where E_0 is the incident beam energy, ΔE is the target thickness, and Γ_1 and Γ_2 are two parameters accounting, respectively, for the slopes of the falling and leading edges of the target profile.

Finally, it is possible to introduce the target profile $P(E)$ into Equation 3.27, to parametrize completely the γ-peak:

$$\left[Y_i\right]_{\text{Exp}} = \left[K\frac{\sigma(E_{p,i})}{\epsilon_{\text{eff}}(E_{p,i})}\eta_{ph}(E_{\gamma,i})P(E_{p,i})F(E_{\gamma,i},\sigma_{\text{HPGe}})\Delta E_{\gamma,i}\right]_{Model} \tag{3.29}$$

By obtaining the yield of each bin of the γ-peak (left part of the equation), it is possible to minimize the difference between them and the model (right part of the equation), where ΔE, E_0, Γ_1, Γ_2, K and σ_{HPGe} are used as minimization parameters. The resolution of the detector, σ_{HPGe}, was considered constant in the γ-peak range. In order to perform this, the Truncated Newton Method was used, provided by the SciPy library [45]. Since the reference runs were performed

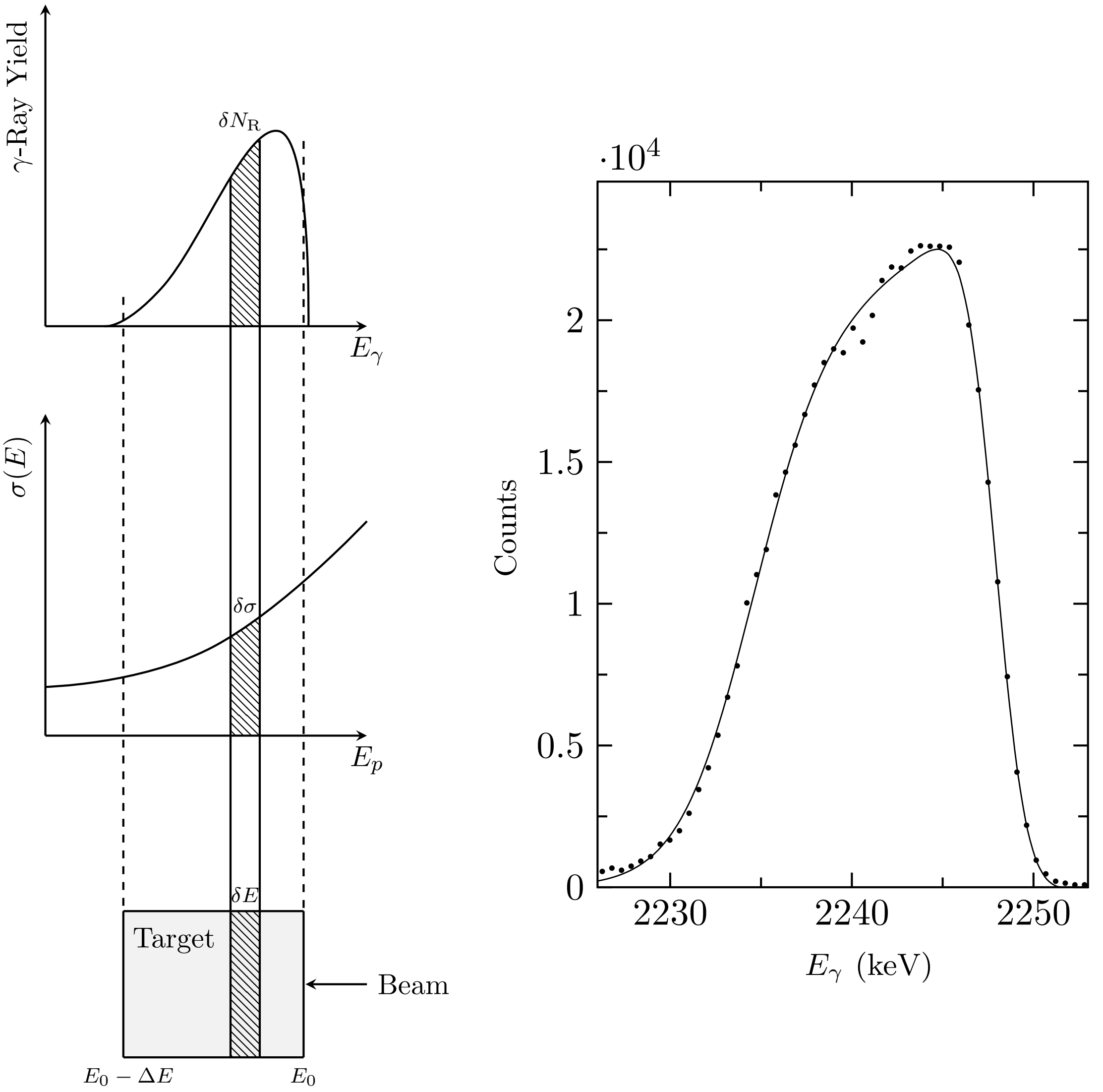

Figure 3.7: Left: The peak shape of the γ-ray emitted reflects the cross section dependence on energy as the beam loses energy inside the target. The number of counts, δN_{R}, corresponding to a thin slice of the target of width, δE, is proportional to the integral of the cross section. Right: Example of the γ-ray peak from the present study of the $^{12}\mathrm{C}(p,\gamma)^{13}\mathrm{N}$ reaction.

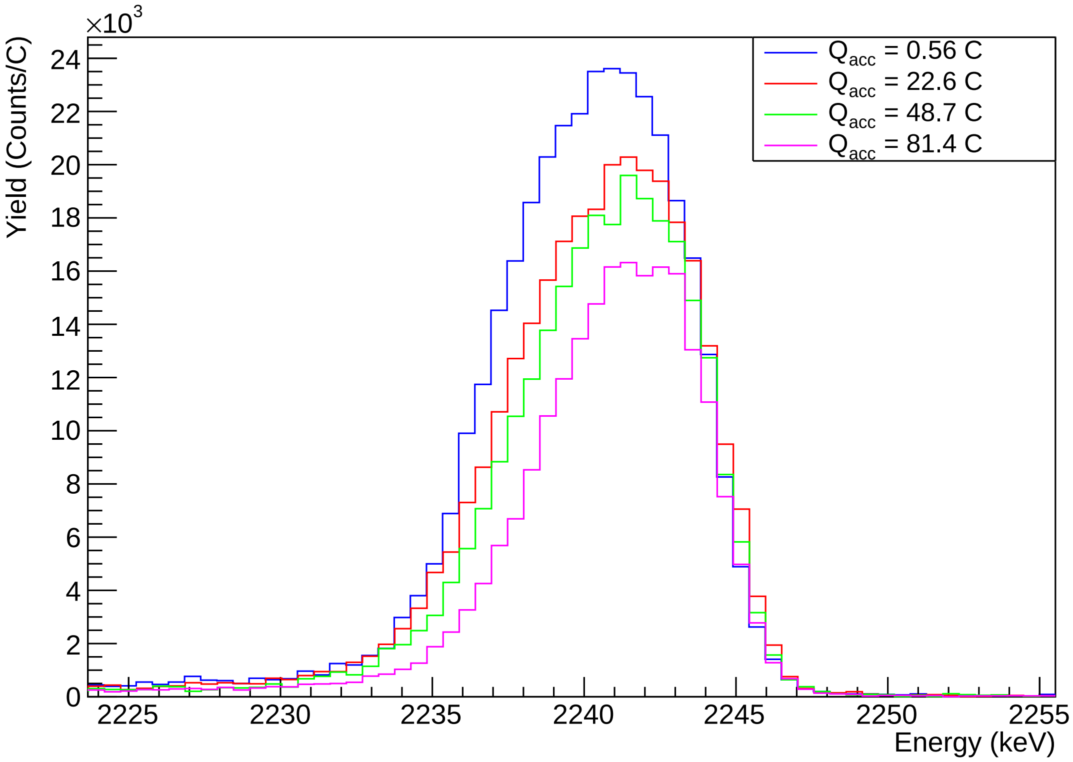

Figure 3.8: Peaks for the *nat3* target ($d = 0$ cm) at $E_p = 378.7$ keV and at different $Q_{\rm acc}$. The spectra are normalized by the integrated charge of each run. The width of the peak changes as the target is degraded by the beam.

both at distances, d, of 1.35 cm and 16.35 cm, two different ΔE are obtained for each accumulated charge $Q_{\rm acc}$. The resulting fits and target profiles can be seen in Fig. 3.9-3.18, where, for each target, the peaks from the first and last reference run at both distances are plotted.

The attained target thicknesses are plotted in Fig. 3.21-3.23 for both the distances. In addition, the ΔE for each target are summarized in Tab. 3.4. One example of all the fit parameters is in Tab. 3.5. The error associated to the accumulated charge $Q_{\rm acc}$ was assumed to be 1%, which is bigger than the one reported in the current integrator datasheet. Indeed, a possible systematic contribution from the human operator of the accelerator had to be taken into account. The error on the ΔE was obtained directly from the minimization procedure. The results for both distances are in good agreement with each other.

Finally, the ΔE shows a strange behaviour up to the second reference run, as no decrease is observed. What is more puzzling is that the target thickness seems to increase in the *nat8* case. One possible explanation could be the following: during the irradiation, the carbon partially diffused into the Ta backing, and thus modified the target composition. In this way, the stopping power of the target increased. Hence the increase in the ΔE. In order to check this hypothesis, additional target studies are needed which are out of scope for the present work.

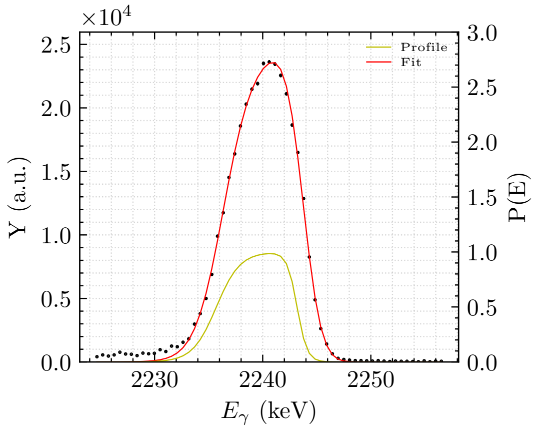

Figure 3.9: First reference run of the *nat3* target at $d = 1.35$ cm ($Q_{\text{acc}} = 0.06$ C).

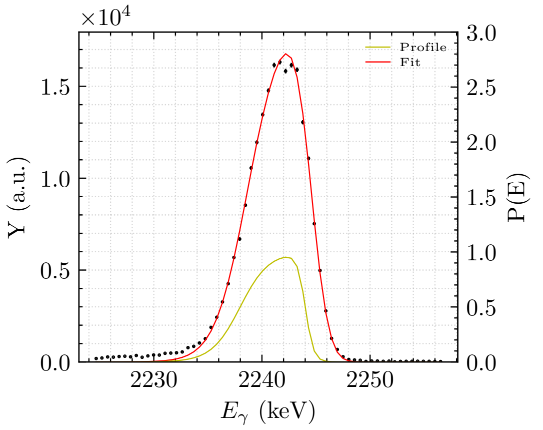

Figure 3.10: Last reference run of the *nat3* target at $d = 1.35$ cm ($Q_{\text{acc}} = 81.41$ C).

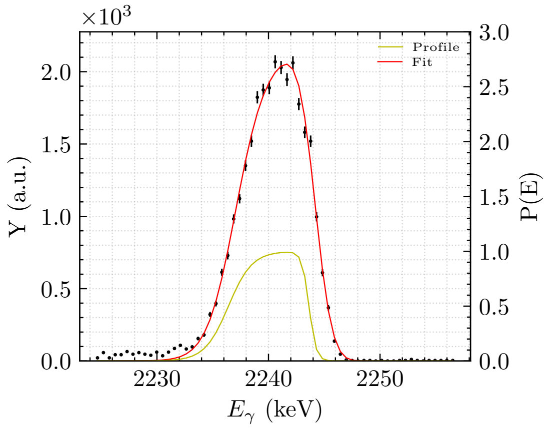

Figure 3.11: First reference run of the *nat3* target at $d = 16.35$ cm ($Q_{\text{acc}} = 0.06$ C).

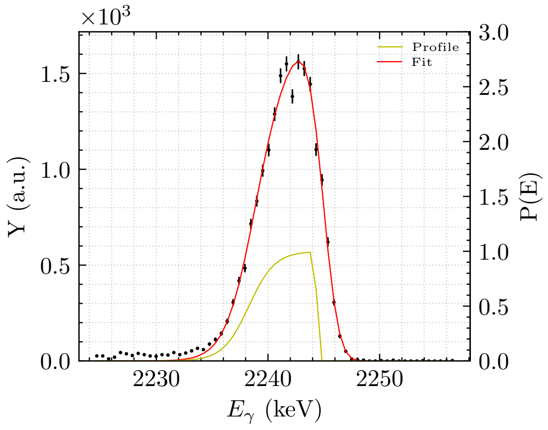

Figure 3.12: Last reference run of the *nat3* target at $d = 16.35$ cm ($Q_{\text{acc}} = 81.41$ C).

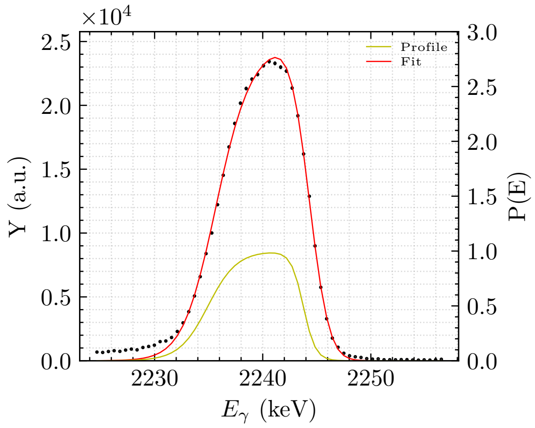

Figure 3.13: First reference run of the *nat4* target at $d = 1.35$ cm ($Q_{\text{acc}} = 0.27$ C).

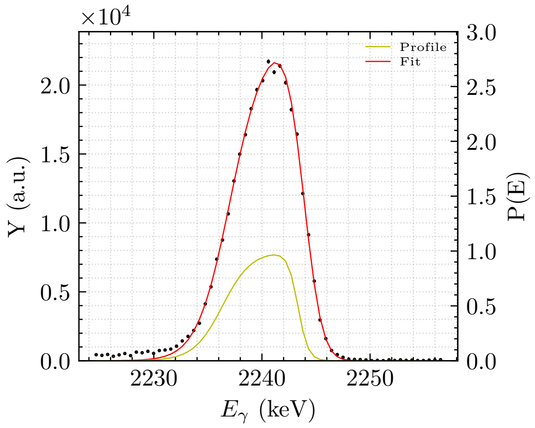

Figure 3.14: Last reference run of the *nat4* target at $d = 1.35$ cm ($Q_{\text{acc}} = 67.63$ C).

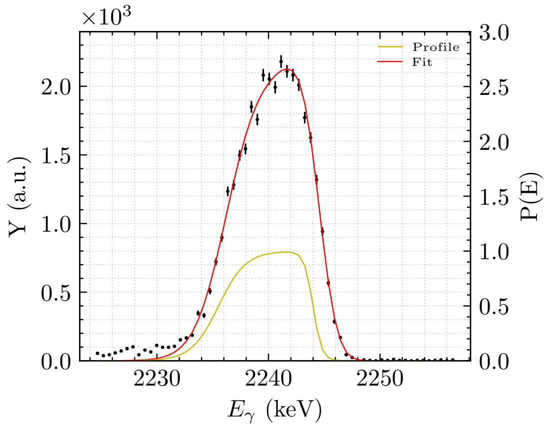

Figure 3.15: First reference run of the *nat4* target at $d = 16.35$ cm ($Q_{\text{acc}} = 0.27$ C).

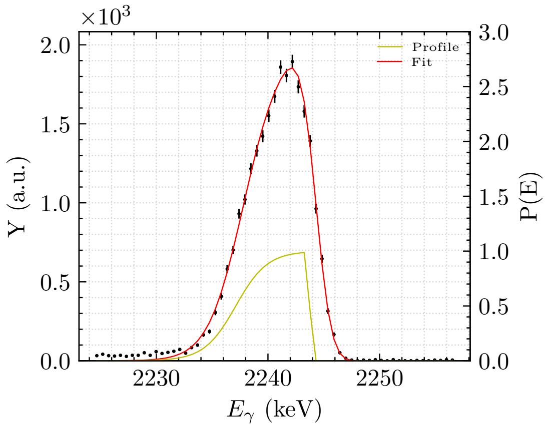

Figure 3.16: Last reference run of the *nat4* target at $d = 16.35$ cm ($Q_{\text{acc}} = 67.63$ C).

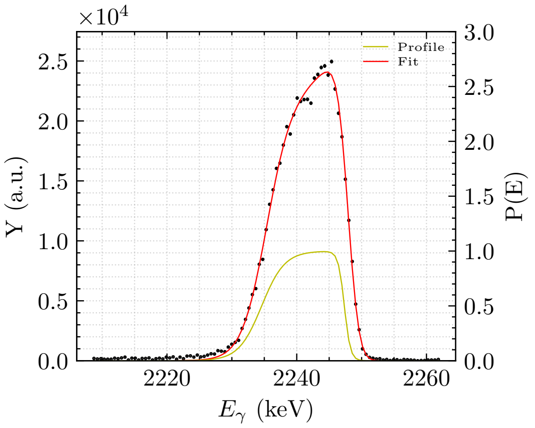

Figure 3.17: First reference run of the *nat8* target at $d = 1.35$ cm ($Q_{\text{acc}} = 0.27$ C).

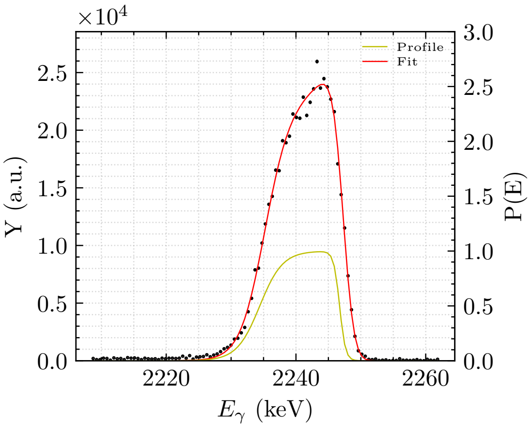

Figure 3.18: Last reference run of the *nat8* target at $d = 1.35$ cm ($Q_{\text{acc}} = 49.74$ C).

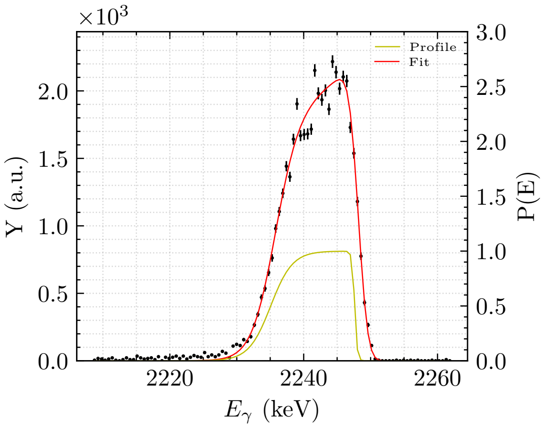

Figure 3.19: First reference run of the *nat8* target at $d = 16.35$ cm ($Q_{\text{acc}} = 0.27$ C).

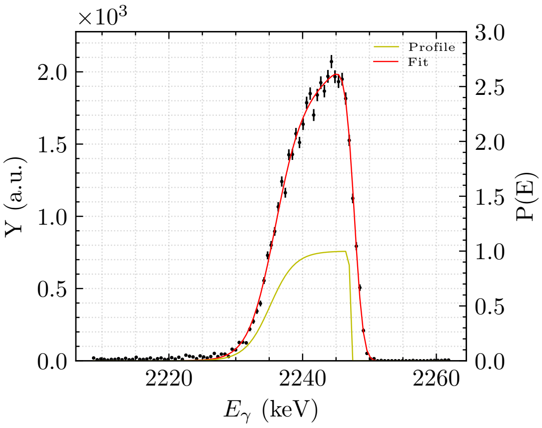

Figure 3.20: Last reference run of the *nat8* target at $d = 16.35$ cm ($Q_{\text{acc}} = 49.74$ C).

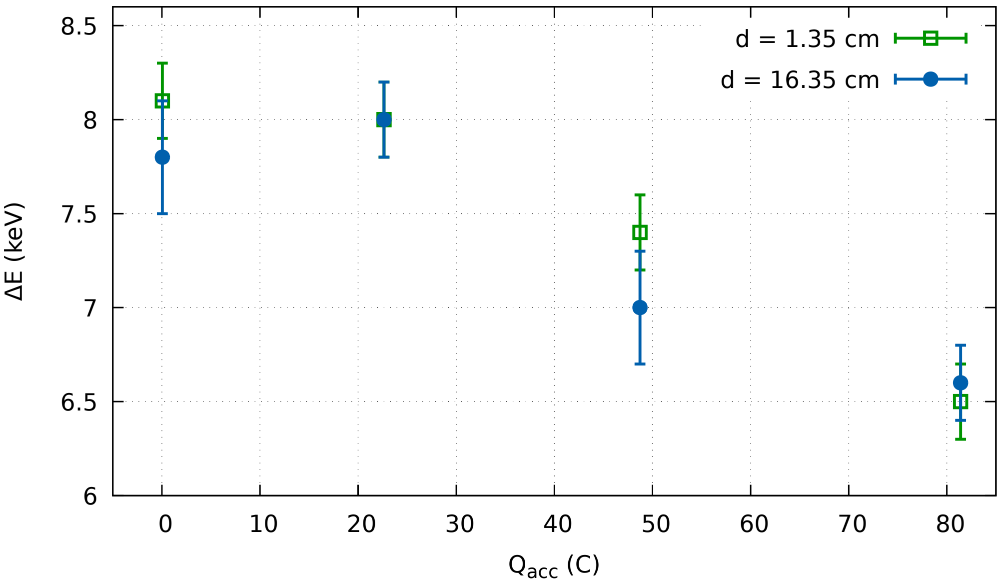

Figure 3.21: ΔE as a function of the accumulated charge on the target (*nat3*).

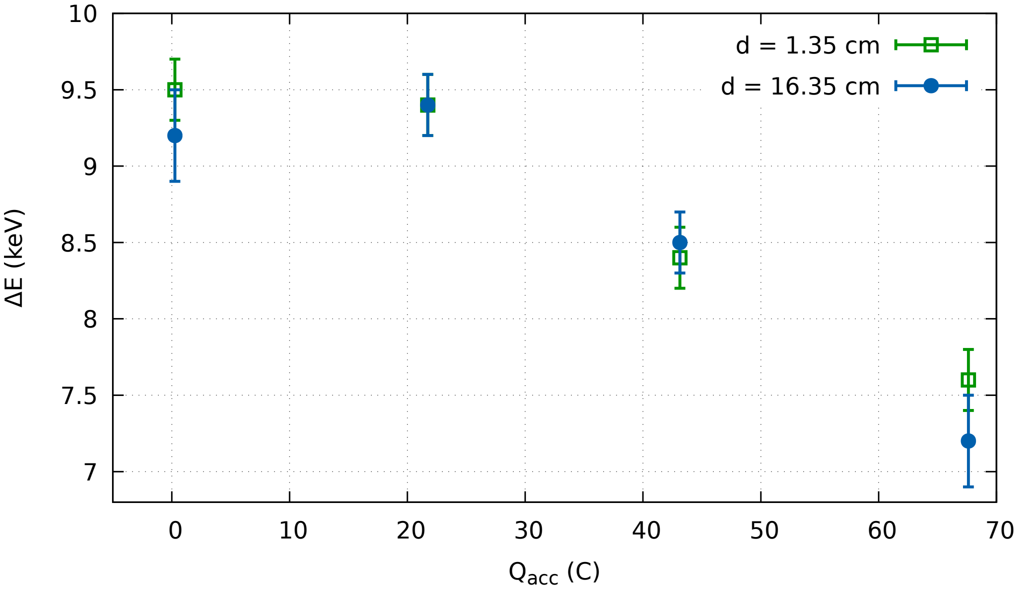

Figure 3.22: ΔE as a function of the accumulated charge on the target (*nat4*).

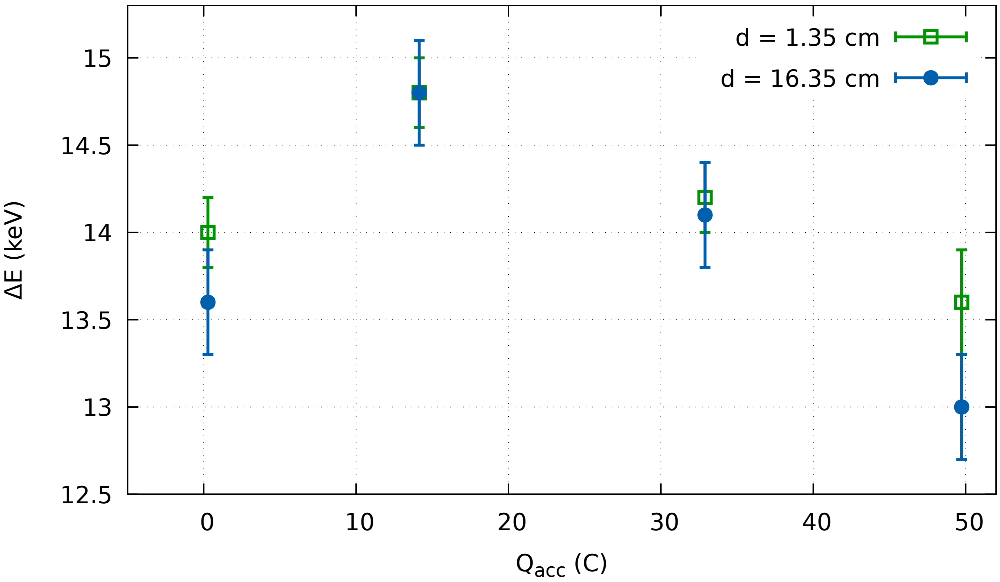

Figure 3.23: ΔE as a function of the accumulated charge on the target (*nat8*).

Target	Q_{acc} C	$\Delta E(d = 1.35\text{cm})$ keV	$\Delta E(d = 16.35\text{cm})$ keV
nat3	0.560(5)	8.1(2)	7.8(3)
	22.6(2)	8.0(2)	8.0(2)
	48.7(5)	7.4(2)	7.0(3)
	81.4(8)	6.5(2)	6.6(2)
nat4	0.271(3)	9.5(2)	9.2(3)
	21.7(2)	9.4(2)	9.4(2)
	43.1(4)	8.4(2)	8.5(2)
	67.6(7)	7.6(2)	7.2(3)
nat8	0.276(3)	14.0(2)	13.6(3)
	14.1(1)	14.8(2)	14.8(3)
	32.9(3)	14.2(2)	14.1(3)
	49.7(5)	13.6(3)	13.0(3)

Table 3.4: Table with the target thicknesses ΔE obtained for each target.

d cm	Q_{acc} C	ΔE keV	K	Γ_1 keV	Γ_2 keV	σ_{HPGe} keV
1.35	0.560(5)	8.1(2)	584(2)	1.13(6)	0.53(1)	1.9(1)
	22.6(2)	8.0(2)	505(4)	1.36(9)	0.18(2)	2.5(3)
	48.7(5)	7.4(2)	450(3)	1.34(8)	0.10(2)	2.6(3)
	81.4(8)	6.5(2)	435(3)	1.43(3)	0.64(8)	1.3(5)
16.35	0.560(5)	7.8(3)	3.62(5)	1.02(9)	0.18(4)	2.3(3)
	22.6(2)	8.0(2)	3.19(6)	1.5(1)	0.27(8)	2.0(4)
	48.7(5)	7.0(3)	3.15(3)	1.43(7)	0.52(8)	1.6(4)
	81.4(8)	6.6(2)	2.79(6)	1.15(5)	0.029(5)	2.1(3)

Table 3.5: Table with all the fit parameters for *nat3* target obtained at different accumulated charges, Q_{acc}.

3.5 Yield Analysis

The net counts in the γ-ray peak, corresponding to the direct capture to the ^{13}N ground state, was obtained from the spectra by choosing the Region of Interest (ROI) that coincides with the range of channels where such counts are expected. The ROI's position is selected based on the high-energy edge of the structure arising over the γ-continuum, which is easy to localize and that corresponded to the maximum energy calculated with the initial beam energy. The extension of the ROI highly depends on the target thickness. In addition, as can be seen in Fig. 3.24-3.25, in case of the thin targets, small tails are located on the low energy side of the peak. In order to take it into account, the ROI was selected in such a way half of the tail is considered. Nevertheless, the contribution of the tail to the net peak count is only of $\sim 1\%$. Furthermore, the tail is not observed in the case of low energy runs ($E_p < 250$ keV).

In case of the *nat8* target, the γ-peak is very feeble, with a very low S/N ratio. In fact, it is only visible in the low-gain channel of the data acquistion chain, which thus was exploited for the analysis of this target. In case of all the other spectra, the high-gain channel was used.

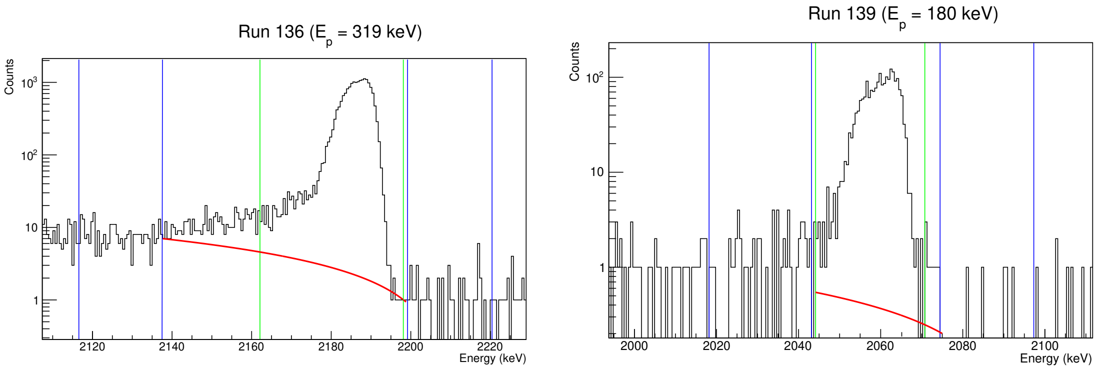

Figure 3.24: Two different peaks for the *nat3* target. The spectrum on the left is shown in logarithmic scale in order to underline the tail on the low energy side. The blue lines indicate the region where the background was estimated. The green lines indicate the integration range. The red line is the calculated background.

The net number of counts is calculated as the total number of counts, N_{T}, less the number of counts in the background, N_{B}, that are determined by the area of the

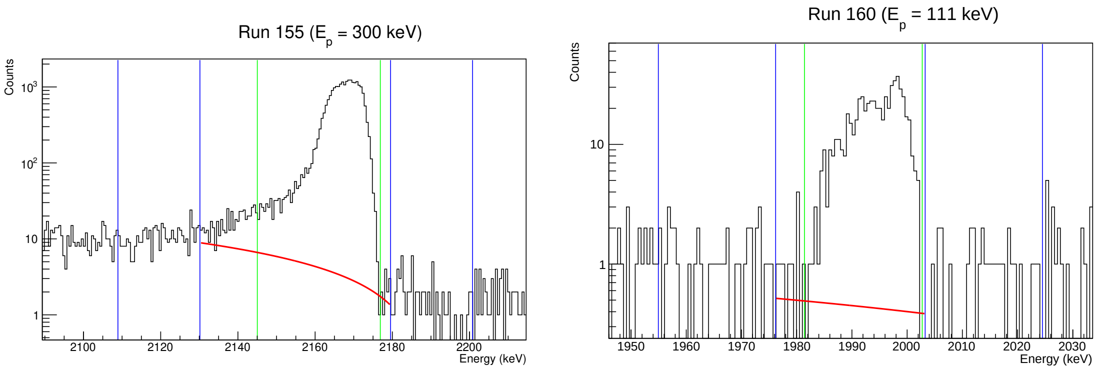

Figure 3.25: Two different peaks for the *nat4* target. The spectrum on the left is showed in logarithmic scale in order to underline the tail on the low energy side. The blue lines indicate the region where the background was estimated. The green lines indicate the integration range. The red line is the calculated background.

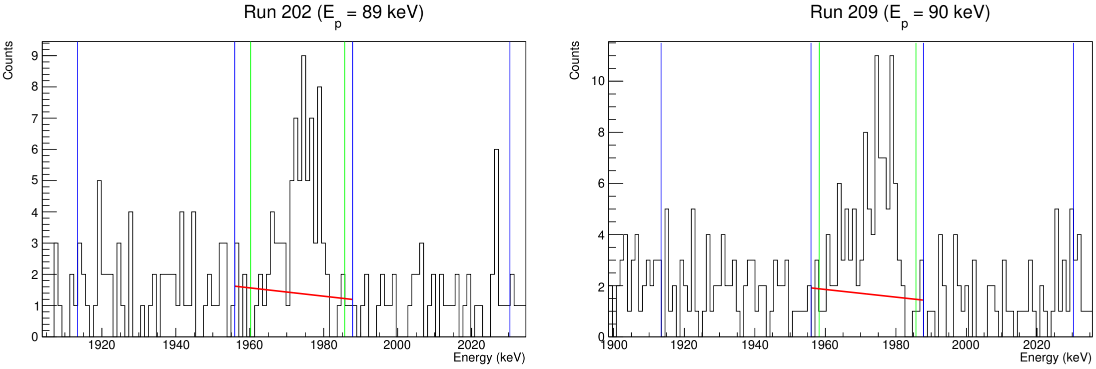

Figure 3.26: Two different peaks for the *nat8* target. The blue lines indicate the region where the background was estimated. The green lines indicate the integration range. The red line is the calculated background.

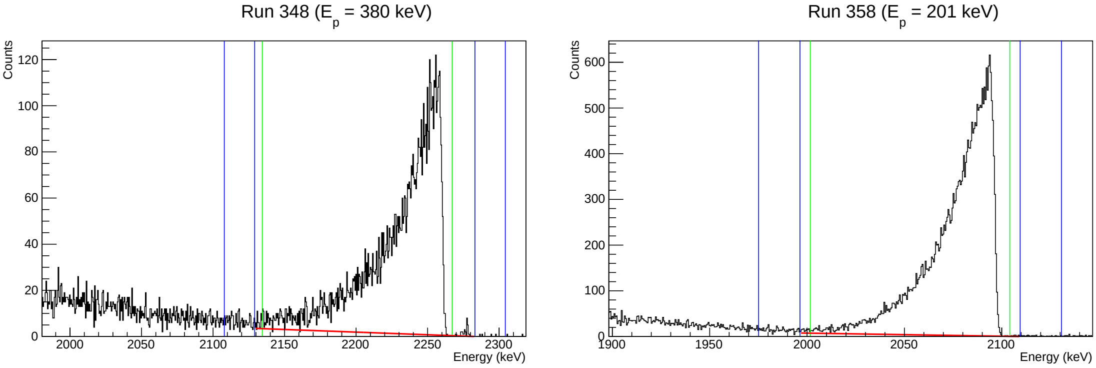

Figure 3.27: Two different peaks for the *graphite* target. The blue lines indicate the region where the background was estimated. The green lines indicate the integration range. The red line is the calculated background.

trapezoid below the γ-peak:

$$N_{\text{counts}} = N_{\text{T}} - N_{\text{B}} \tag{3.30}$$

$$\sigma^2_{\text{counts}} = \sigma^2_{\text{T}} + \sigma^2_{\text{B}} \tag{3.31}$$

where σ_{counts} is the calculated statistical error, and σ_{T} and σ_{B} are respectively the error of the peak counts and the error of the background counts, calculated assuming a Poissonian distribution.

The N_{counts} is corrected for the dead time of the acquisition, which is the time after each event during which the system is not able to record the following one. It can be estimated thanks to the MAESTRO [46] software used for the data acquisition. It provides the evaluation of the live time, t_{live}, and of the real time, t_{real}, for each acquistion run. Hence, the corrected number of counts inside the γ-peak is calculated as:

$$N_{\text{counts, corr}} = N_{\text{counts}} \frac{t_{\text{real}}}{t_{\text{live}}} \tag{3.32}$$

The acquisition runs most affected by this problem are the high energy ones ($E_p >$ 250 keV), due to higher counting rates. In fact, the correction is $\sim$ 6-7% for each of these. In case of the lower energy runs, the correction is approximately 2-1%.

In order to calculate the reaction yield the number of incoming protons, N_p, had to be calculated using the following:

$$N_p = \frac{Q_{\text{run}}}{q_e} \tag{3.33}$$

where the Q_{run} is the accumulated charge during each experimental run, and q_e is the elementary charge. Before each analysis, the consistency of the charge measurement was checked by comparing the counts in the MCA counter with the NIM counter located in the control room.

The yields are then calculated using Equation 3.1. The obtained results for the long runs can be visualized in Fig. 3.28 and are listed in Tab. 3.6. The reported yield errors are only the statistical ones. The energy uncertainty was assumed to be 0.1 keV [34] for all the energies. The E_{CM} was calculated as:

$$E_{\text{CM}} = \frac{M}{M+m} E_{\text{beam}} \tag{3.34}$$

where M is the mass of the ^{12}C and m is the mass of the proton.

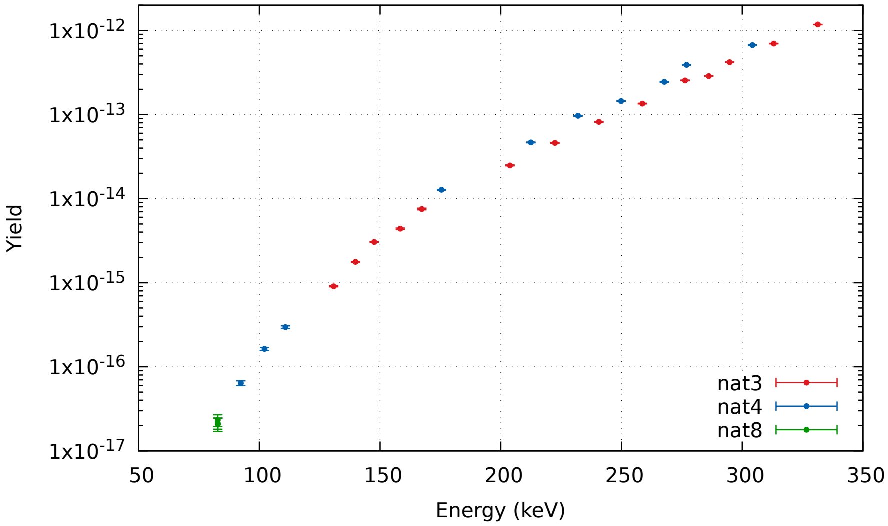

Figure 3.28: Long runs yields in function of the beam energy in CM frame for all the thin targets. The graphite target is omitted as presents much higher yields because of its thickness.

The yields of the *nat4* target are higher than the one of the *nat3*: this could be attributed to the difference in thickness of the two, as the former is slightly thicker (Section 3.4). The same applies for the *graphite*, as it can be considered, with a good approximation, infinitely thick i.e. the beam is entirely stopped inside the target.

3.5.1 Reference Runs

The reference runs were mainly analyzed online in order to obtain some initial insight into target degradation, as explained in the Section 2.3. In addition, being done both at 1.35 cm and at 16.35 cm, they can also gives hints about the setup geometry, e.g. if either the target or the detector positioning is troublesome.

The calculated yields at both distances, plotted as a function of the total accumulated charge on the target, Q_{acc}, can be seen in Fig. 3.29-3.31. In addition, the results are listed in Tab. 3.7-3.9. The measurementes at the two distances are only compatible for the *nat4* target: the discrepancy between the two values is $\sim$ 2%. On the contrary, in case of the *nat3* target, some inconsistencies of unknown nature appear between the two measurements as the discrepancy goes up to $\sim$ 10%. This problem must be addressed in the future and is not the goal of this work.

Target	E_{CM} keV	Yield
nat3	130.8(1)	$9.1(2) \times 10^{-16}$
	139.8(1)	$1.77(2) \times 10^{-15}$
	147.6(1)	$3.05(3) \times 10^{-15}$
	158.4(1)	$4.40(8) \times 10^{-15}$
	167.3(1)	$7.53(2) \times 10^{-15}$
	203.9(1)	$2.49(3) \times 10^{-14}$
	222.5(1)	$4.61(5) \times 10^{-14}$
	240.7(1)	$8.18(9) \times 10^{-14}$
	258.7(1)	$1.35(1) \times 10^{-13}$
	276.3(1)	$3.06(2) \times 10^{-13}$
	286.1(1)	$2.87(2) \times 10^{-13}$
	294.8(1)	$4.20(3) \times 10^{-13}$
	313.1(1)	$7.00(5) \times 10^{-13}$
	331.3(1)	$1.179(6) \times 10^{-12}$
nat8	82.8(1)	$2.1(3) \times 10^{-17}$
	82.8(1)	$2.1(4) \times 10^{-17}$
	82.8(1)	$2.3(4) \times 10^{-17}$

Target	E_{CM} keV	Yield
nat4	92.3(1)	$6.4(4) \times 10^{-17}$
	102.1(1)	$1.63(7) \times 10^{-16}$
	110.8(1)	$3.0(1) \times 10^{-16}$
	175.5(1)	$1.27(1) \times 10^{-14}$
	212.5(1)	$4.66(5) \times 10^{-14}$
	232.0(1)	$9.67(9) \times 10^{-14}$
	249.8(1)	$1.44(1) \times 10^{-13}$
	267.7(1)	$2.45(2) \times 10^{-13}$
	277.0(1)	$3.90(3) \times 10^{-13}$
	304.3(1)	$6.70(6) \times 10^{-13}$
graphite	350.6(1)	$9.6(1) \times 10^{-12}$
	350.6(1)	$9.24(8) \times 10^{-12}$
	350.6(1)	$9.38(6) \times 10^{-12}$
	350.6(1)	$9.44(5) \times 10^{-12}$
	350.6(1)	$9.39(4) \times 10^{-12}$
	350.6(1)	$9.30(4) \times 10^{-12}$
	350.6(1)	$9.24(3) \times 10^{-12}$
	350.6(1)	$9.23(7) \times 10^{-12}$
	350.6(1)	$9.21(1) \times 10^{-12}$
	184.5(1)	$3.73(2) \times 10^{-14}$

Table 3.6: Table with the calculated yields of the long runs for each target.

Position cm	Q_{acc} C	Yield
1.35	0.0560(5)	$2.43(2) \times 10^{-12}$
	0.0784(7)	$2.44(3) \times 10^{-12}$
	22.6(2)	$2.10(1) \times 10^{-12}$
	48.7(5)	$1.86(1) \times 10^{-12}$
	81.4(8)	$1.504(7) \times 10^{-12}$

Position cm	Q_{acc} C	Yield
16.35	0.355(4)	$2.61(3) \times 10^{-12}$
	22.8(2)	$2.35(3) \times 10^{-12}$
	48.9(5)	$2.06(3) \times 10^{-12}$
	81.9(8)	$1.75(2) \times 10^{-12}$

Table 3.7: Tables with the calculated yields of the reference runs at both distances for the *nat3* target.

Finally, the most problematic target is the *nat8*: in fact, the second and the third reference runs seems to be affected by erroneous positioning of the detector. This is confirmed by an entry in the logbook of the WG: it is reported that the Pb shielding was a few centimeters downstream of its original position. It is unkown since when the problem arised: from the results it seems that both the second and the third set of runs were afflicted. This could make the first and the second long runs of this target of dubious value.

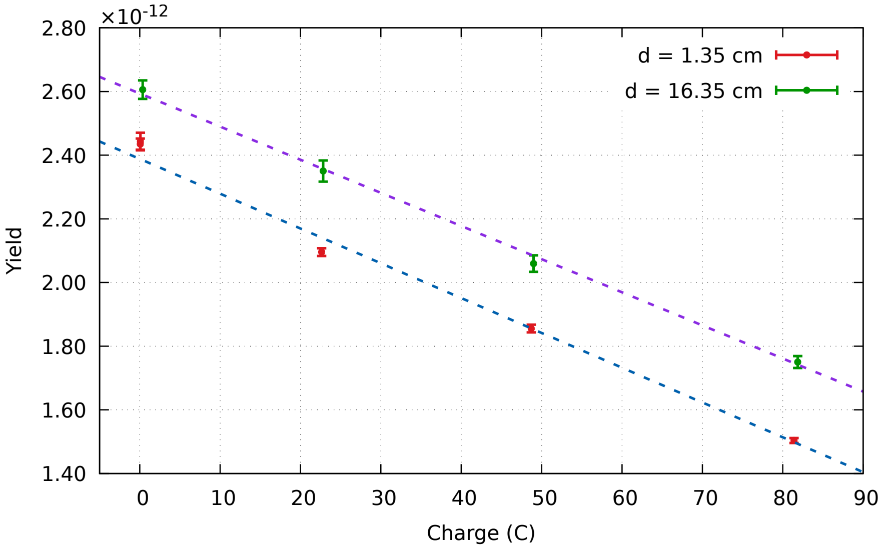

Figure 3.29: Reference runs yields as a function of the accumulated charge for *nat3* target. The yields were corrected for the different efficiencies at the two distances.

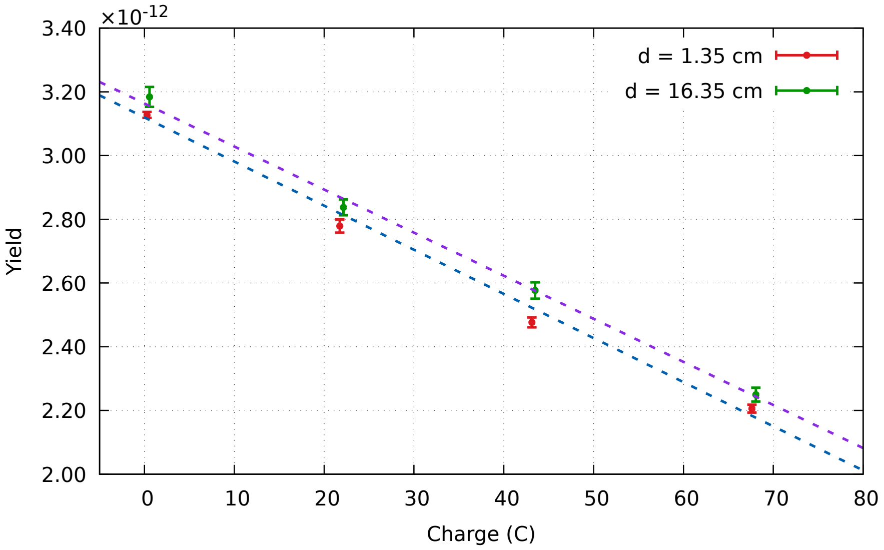

Figure 3.30: Reference runs yields as a function of the accumulated charge for *nat4* target. The yields were corrected for the different efficiencies at the two distances.

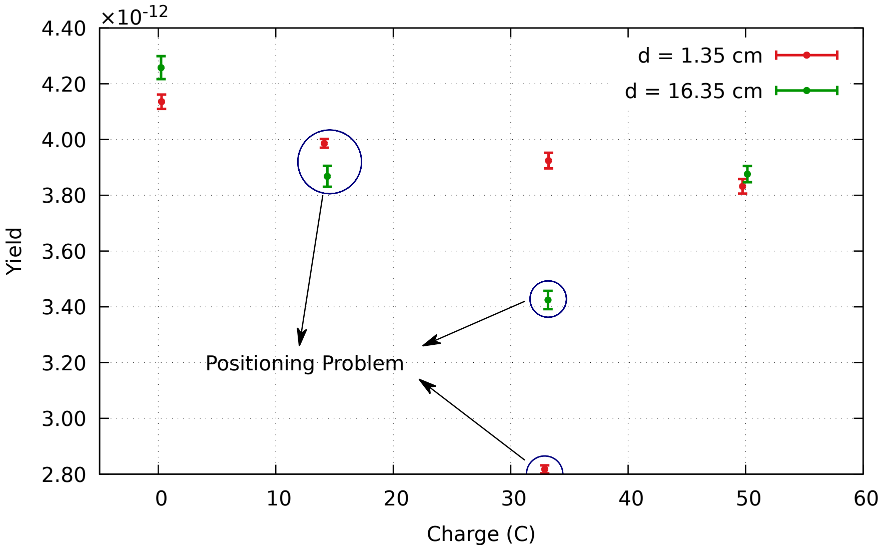

Figure 3.31: Reference runs yields as a function of the accumulated charge for *nat8* target. The yields were corrected for the different efficiencies at the two distances.

Position cm	Q_acc C	Yield
1.35	0.271(3)	$3.127(9) \times 10^{-12}$
	21.7(2)	$2.78(2) \times 10^{-12}$
	43.1(4)	$2.48(2) \times 10^{-12}$
	67.6(7)	$2.21(1) \times 10^{-12}$

Position cm	Q_acc C	Yield
16.35	0.565(6)	$3.18(3) \times 10^{-12}$
	22.1(2)	$2.84(3) \times 10^{-12}$
	43.5(4)	$2.58(3) \times 10^{-12}$
	68.1(7)	$2.25(2) \times 10^{-12}$

Table 3.8: Tables with the calculated yields of the reference runs at both distances for the *nat4* target.

Position cm	Q_acc C	Yield
1.35	0.276(3)	$4.14(3) \times 10^{-12}$
	14.1(1)	$3.99(2) \times 10^{-12}$
	32.9(3)	$2.82(1) \times 10^{-12}$
	33.2(3)	$3.92(3) \times 10^{-12}$
	49.7(5)	$3.83(3) \times 10^{-12}$

Position cm	Q_acc C	Yield
16.35	0.230(2)	$4.26(4) \times 10^{-12}$
	14.4(1)	$3.87(4) \times 10^{-12}$
	33.2(3)	$3.42(3) \times 10^{-12}$
	50.2(5)	$3.88(3) \times 10^{-12}$

Table 3.9: Tables with the calculated yields of the reference runs at both distances for the *nat8* target.

3.6 S-factor Calculation

The S-factor was calculated using Equation 3.3. The effective energy, E_{eff}, was found using the Equation 3.4. The ΔE was obtained by linearly interpolating the two consecutive values obtained from the Peak Shape Analysis (Section 3.4), and calculating its value at the accumulated charge, Q_{acc}, of a given run. In case of the *graphite* target, the $\Delta E \sim E_{\text{CM}}$ was assumed. The stopping power was obtained according to Equation 3.11 and its uncertainty was derived from SRIM tables. The results can be seen in Fig. 3.32 and are listed in in Tab. 3.10. The reported errors include only the statistical contribution, i.e. coming from the counting statistics. The systematic uncertainties are listed in Tab. 3.11. The largest contribution comes from the uncertainty on the target thickness.

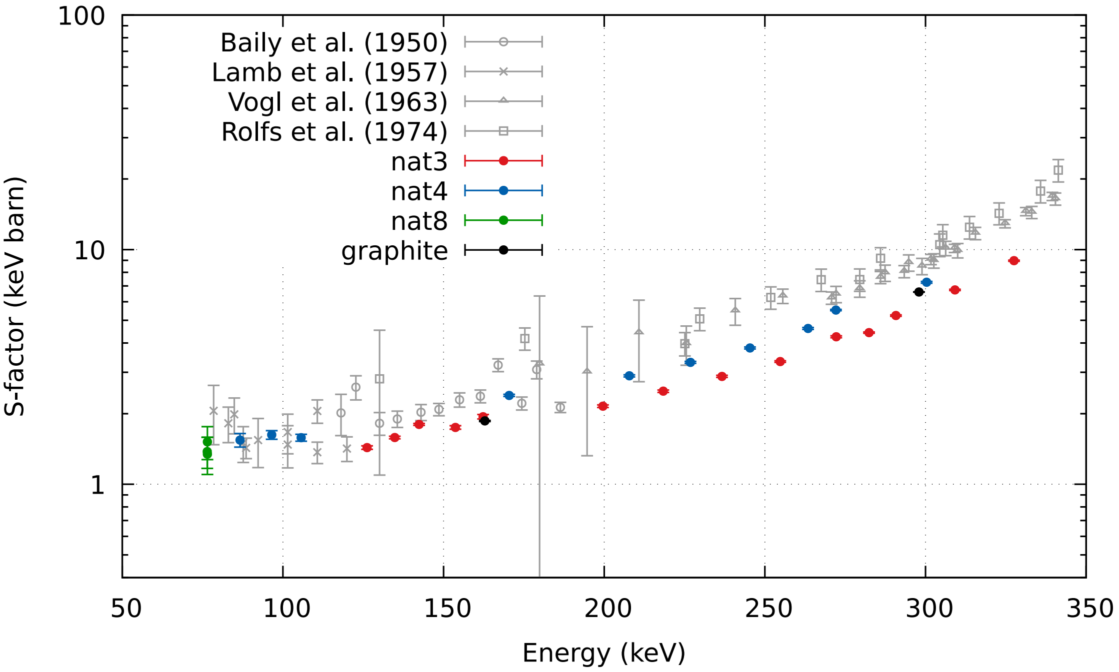

Figure 3.32: S-factor results. The reported uncertainty includes only the statistical contribution. Only two point of the *graphite* target were plotted for better visualization.

In case of higher energies ($E_{\text{eff}} \geq 150$ keV), the results are lower than the literature data: the discrepancy is of $\sim 20\%$ for the *nat4*, and $\sim 50\%$ for the *nat3* target. In addition, the collected values seem to be lower for the runs performed at higher accumulated charge on the target, e.g. the $E_{\text{eff}} = 153.7$ keV and $E_{\text{eff}} = 282.4$ keV runs for the *nat3* target which were executed at $Q_{\text{acc}} \geq 23$ C. This could suggest

Target	E_{eff} keV	S-factor keV barn
nat3	126.2(1)	1.43(2)
	134.8(1)	1.58(2)
	142.4(1)	1.80(2)
	153.7(1)	1.75(3)
	162.3(1)	1.94(4)
	199.6(1)	2.15(3)
	218.4(1)	2.49(3)
	236.6(1)	2.88(3)
	254.8(1)	3.34(3)
	272.2(1)	4.25(4)
	282.4(1)	4.43(3)
	290.8(1)	5.24(4)
	309.2(1)	6.73(4)
	327.6(1)	8.97(5)
nat8	76.4(1)	1.4(2)
	76.5(1)	1.3(2)
	76.5(1)	1.5(2)

Target	E_{eff} keV	S-factor keV barn
nat4	86.7(1)	1.5(1)
	96.5(1)	1.62(7)
	105.6(1)	1.58(5)
	170.4(1)	2.39(2)
	207.8(1)	2.90(3)
	226.8(1)	3.31(3)
	245.4(1)	3.81(4)
	263.4(1)	4.61(4)
	272.1(1)	5.52(4)
	300.3(1)	7.26(6)
graphite	298.0(1)	6.77(7)
	298.0(1)	6.53(5)
	298.0(1)	6.62(5)
	298.0(1)	6.67(4)
	298.0(1)	6.63(3)
	298.0(1)	6.54(2)
	298.0(1)	6.52(2)
	298.0(1)	6.52(5)
	298.0(1)	6.511(9)
	162.9(1)	1.86(1)

Table 3.10: Table with the calculated S-factors for all the targets. The reported uncertainty includes only the statistical contribution.

Source	Systematic (%)
Photo-peak Efficiency	5%
Stopping Power	6.4% [40]
Beam Energy	1%
Charge Integration	1%
Target Thickness	7%

Table 3.11: Systematic uncertainties (percentage) for the present measurements of the $^{12}\text{C}(p,\gamma)^{13}\text{N}$ reaction.

an important variation in the target stoichiometry. In fact, if some of the ^{12}C has diffused into the Ta backing, the ϵ_{eff} would increase and thus the calculated S-factor would be bigger.

As discussed in Section 3.4, the target characterisation is the main issue of the present analysis. An intense investigation of this aspect is planned for the second half of 2020 and was not possible during this work due to the COVID-19 contingency. In particular, the slight disagreement between the *nat4* and *nat3* results should be investigated. In addition, a new experiment, characterized by the activation technique detecting the 511 keV γ-rays from the ^{13}N decay in coincidence is planned in order to obtain the S-factor in a quite independent way. Despite the above mentioned problems, the trend of the S-factor follows the values reported in literature and the present analysis confirmed the possibility to investigate the S-factor with unprecedented low uncertainties by going in an underground laboratory.

Conclusions

The ^{12}C$(p,\gamma)^{13}$N reaction, which is the first reaction of the CNO cycle, affects the ratio of abundances of the C isotopes inside the star interiors. In particular, it has very important impact during the dredge-up episodes, i.e. mixing events due to convective motion inside the stars, that occur at the end of the hydrogen burning, when the star enters its *RGB* phase, and at the end of the helium burning phase, when the *AGB* phase starts. Determining the rate of the ^{12}C$(p,\gamma)^{13}$N reaction is therefore critical to produce accurate theoretical models of the complex mixing mechanisms inside the stars.

This thesis has reported on the experimental study to measure the S-factor of the ^{12}C$(p,\gamma)^{13}$N reaction at lowest energies accessible by means of an HPGe detector. The measurements were carried out at the LNGS underground facility, where the unique low level of γ-ray background has allowed for the precise detection of prompt γ-rays associated to the direct capture component of the studied reaction. The efficiency of the detector was obtained using ^{137}Cs and ^{60}Co sources, and the ^{14}N$(p,\gamma)^{15}$O resonance at $E_p = 278$ keV. The Peak Shape Analysis was performed on the prompt γ-peak in order to extract the information about target thickness at different points of the accumulated charge, Q_{acc}. Finally, the non-resonant S-factor was obtained in the energy range $E_{\mathrm{cm}} \approx 75 - 350$ keV.

The performed analysis is an initial attempt for the derivation of the ^{12}C$(p,\gamma)^{13}$N S-factor. Further work is necessary in order to improve the results and investigate the discrepancy between the obtained S-factors and the literature data. In fact, some problems with the target composition and setup geometry have been underlined in Section 3.5.1 and Section 3.6. These must be addressed and studied more thoroughly in the ongoing analysis and future data taking campaigns already planned at the LUNA experiment. Nevertheless, the present work showed how it is possible at LUNA to measure the ^{12}C$(p,\gamma)^{13}$N cross section directly at the energies of astrophysical interest with unprecedented high sensitivity.

Bibliography

[1] M. D. Shetrone, “Magnesium and Carbon isotopes in Globular Cluster Giants. Test of Deep Mixing. II.,” *Astrophysical Journal*, vol. 112, p. 2639, Dec. 1996.

[2] P. Hoppe, S. Amari, E. Zinner, T. Ireland , and R. S. Lewis, “Carbon, Nitrogen, Magnesium, Silicon, and Titanium Isotopic Compositions of Single Interstellar Silicon Carbide Grains from the Murchison Carbonaceous Chondrite,” *Astrophysical Journal*, vol. 430, p. 870, Aug. 1994.

[3] R. Claus E. and R. William S., *Cauldrons in the Cosmos: Nuclear Astrophysics.* University Of Chicago Press, 1988.

[4] E. Burbidge, G. Burbidge, W. Fowler, and F. Hoyle, “Synthesis of the Elements in Stars,” *Reviews of Modern Physics*, vol. 29, pp. 547–650, October 1957.

[5] A. G. W. Cameron, “Abundances of the elements in the solar system,” *Space Science Reviews*, vol. 15, September 1973.

[6] D. Clayton, *Handbook of Isotopes in the Cosmos: Hydrogen to Gallium.* Cambridge University Press, 2003.

[7] H. A. Bethe, “Energy Production in Stars,” *Phys. Rev.*, vol. 55, pp. 434–456, Mar 1939.

[8] M. Wiescher, “The History and Impact of the CNO Cycles in Nuclear Astrophysics,” *Physics in Perspective*, vol. 20, 02 2018.

[9] C. Iliadis, *Nuclear Physics of Stars.* Wiley-VCH, 2007.

[10] “Cococubed.” `http://cococubed.asu.edu/code_pages/burn_hydrogen.shtml`. Accessed: 2020-07-19.

[11] C. W. Cook, W. A. Fowler, C. C. Lauritsen, and T. Lauritsen, “B^{12}, C^{12}, and the Red Giants,” *Phys. Rev.*, vol. 107, pp. 508–515, Jul 1957.

[12] C. Savage, A. J. Apponi, and L. M. Ziurys, “Galactic $^{12}C/^{13}C$ Ratios From mm-Wave Observations of Interstellar CN,” in *American Astronomical Society Meeting Abstracts #198*, vol. 198 of *American Astronomical Society Meeting Abstracts*, p. 59.13, May 2001.

[13] C. Sneden, “CNO Abundances of Stars Undergoing First Dredge up Mixing,” in *Evolution of Stars: the Photospheric Abundance Connection* (G. Michaud and A. V. Tutukov, eds.), vol. 145 of *IAU Symposium*, p. 235, Jan. 1991.

[14] P. Denissenkov and A. Weiss, “Globular Cluster Archaeology: Hydrogen-burning Nucleosynthesis and Extra Mixing in Extinct Stars,” *The Astrophysical Journal*, vol. 603, p. 119, 12 2008.

[15] O. Straniero, R. Gallino, and S. Cristallo, “s process in low-mass asymptotic giant branch stars,” *Nuclear Physics A*, vol. 777, pp. 311 – 339, 2006. Special Isseu on Nuclear Astrophysics.

[16] R. Wing, “The Carbon Star Phenomenon,” *Proceedings of The International Astronomical Union*, vol. 177, 01 2000.

[17] K. Lodders, H. Palme, and H. P. Gail, “Abundances of the Elements in the Solar System,” *Landolt-Börnstein*, vol. 4B, p. 712, Jan. 2009.

[18] J. M. Trigo-Rodriguez, D. A. Garcia-Hernandez, M. Lugaro, A. I. Karakas, M. van Raai, P. G. Lario, and A. Manchado, “The Role of Massive AGB Stars in the Early Solar System Composition,” *Meteorit. Planet. Sci.*, vol. 44, p. 627, 2009.

[19] S. Mikolaitis, G. Tautvaisiene, R. Gratton, A. Bragaglia, and E. Carretta, “C, N, O abundances and carbon isotope ratios in evolved stars of the open clusters Collinder 261 and NGC 6253,” *Astronomy and Astrophysics*, vol. 541, 03 2012.

[20] N. Langer, A. Heger, S. Wellstein, and F. Herwig, “Mixing and nucleosynthesis in rotating TP-AGB stars,” *Astronomy and Astrophysics*, vol. 346, pp. L37–L40, June 1999.

[21] D. Vescovi, S. Cristallo, M. Busso, and N. Liu, "Magnetic-buoyancy Induced Mixing in AGB Stars: Presolar SiC Grains," *The Astrophysical Journal Letters*, vol. 897, 06 2020.

[22] P. A. Denissenkov and C. A. Tout, "Partial mixing and formation of the ^{13}C pocket by internal gravity waves in asymptotic giant branch stars," *Monthly Notices of the Royal Astronomical Society*, vol. 340, pp. 722–732, 04 2003.

[23] C. L. Bailey and W. R. Stratton, "Cross Section of the $\mathrm{C}^{12}(p,\gamma)\mathrm{N}^{13}$ Reaction at Low Energies," *Phys. Rev.*, vol. 77, pp. 194–196, Jan 1950.

[24] R. N. Hall and W. A. Fowler, "The Cross Section for the Radiative Capture of Protons by C^{12} near 100 Kev," *Phys. Rev.*, vol. 77, pp. 197–204, Jan 1950.

[25] W. A. S. Lamb and R. E. Hester, "Radiative Capture of Protons in Carbon from 80 to 126 kev," *Phys. Rev.*, vol. 107, pp. 550–553, Jul 1957.

[26] J. L. Vogl, *Radiative capture of protons by ^{12}C and ^{13}C below 700 keV*. PhD thesis, California Institute of Technology, 1 1963.

[27] C. Rolfs and R. Azuma, "Interference effects in $^{12}\mathrm{C}(p,\gamma)^{13}\mathrm{N}$ and direct capture to unbound states," *Nuclear Physics A*, vol. 227, no. 2, pp. 291 – 308, 1974.

[28] C. Broggini, "The Luna experiment," *EPJ Web of Conferences*, vol. 136, p. 01008, 01 2017.

[29] `https://www.lngs.infn.it/en/lngs-overview`. Accessed: 2020-05-12.

[30] C. Broggini, D. Bemmerer, A. Caciolli, and D. Trezzi, "LUNA: Status and prospects," *Progress in Particle and Nuclear Physics*, vol. 98, p. 55–84, Jan 2018.

[31] D. Bemmerer, F. Confortola, A. Lemut, R. Bonetti, C. Broggini, P. Corvisiero, H. Costantini, J. Cruz, A. Formicola, Z. Fülöp, G. Gervino, A. Guglielmetti, C. Gustavino, G. Gyürky, G. Imbriani, A. Jesus, M. Junker, B. Limata, R. Menegazzo, and A. Vomiero, "Feasibility of low-energy radiative-capture experiments at the LUNA underground accelerator facility," *European Physical Journal A*, vol. 24, pp. 313–319, 05 2005.

[32] A. Caciolli, L. Agostino, D. Bemmerer, R. Bonetti, C. Broggini, F. Confortola, P. Corvisiero, H. Costantini, Z. Elekes, A. Formicola, Z. Fülöp, G. Gervino, A. Guglielmetti, C. Gustavino, G. Gyürky,

G. Imbriani, M. Junker, M. Laubenstein, and H. Trautvetter, "Ultra-sensitive in-beam γ-ray spectroscopy for nuclear astrophysics at LUNA," *European Physical Journal A*, vol. 39, pp. 179–186, 02 2009.

[33] T. Szücs, D. Bemmerer, C. Broggini, A. Caciolli, F. Confortola, P. Corvisiero, Z. Elekes, A. Formicola, Z. Fülöp, G. Gervino, A. Guglielmetti, C. Gustavino, G. Gyürky, G. Imbriani, M. Junker, A. Lemut, M. Marta, C. Mazzocchi, and H. Trautvetter, "An actively vetoed Clover-detector for nuclear astrophysics at LUNA," *European Physical Journal A*, vol. 44, pp. 513–519, 06 2010.

[34] A. Formicola, G. Imbriani, M. Junker, D. Bemmerer, R. Bonetti, C. Broggini, C. Casella, P. Corvisiero, H. Costantini, G. Gervino, C. Gustavino, A. Lemut, P. Prati, V. Roca, C. Rolfs, M. Romano, D. Schürmann, F. Strieder, F. Terrasi, H.-P. Trautvetter, and S. Zavatarelli, "The LUNA II 400kV accelerator," *Nuclear Instruments and Methods in Physics Research Section A: Accelerators, Spectrometers, Detectors and Associated Equipment*, vol. 507, no. 3, pp. 609 – 616, 2003.

[35] D. Scott, *Underground study of the* $^{17}O(p,\gamma)^{18}F$ *reaction at Gamow energies for classical novae.* PhD thesis, 11 2014.

[36] A. Boeltzig, A. Best, G. Imbriani, M. Junker, M. Aliotta, D. Bemmerer, C. Broggini, C. G. Bruno, R. Buompane, A. Caciolli, F. Cavanna, T. Chillery, G. F. Ciani, P. Corvisiero, L. Csedreki, T. Davinson, R. J. deBoer, R. Depalo, A. D. Leva, Z. Elekes, F. Ferraro, E. M. Fiore, A. Formicola, Z. Fülöp, G. Gervino, A. Guglielmetti, C. Gustavino, G. Gyürky, I. Kochanek, R. Menegazzo, V. Mossa, F. R. Pantaleo, V. Paticchio, R. Perrino, D. Piatti, P. Prati, L. Schiavulli, K. Stöckel, O. Straniero, F. Strieder, T. Szücs, M. P. Takács, D. Trezzi, M. Wiescher, and S. Zavatarelli, "Improved background suppression for radiative capture reactions at LUNA with HPGe and BGO detectors," *Journal of Physics G: Nuclear and Particle Physics*, vol. 45, p. 025203, jan 2018.

[37] G. F. Ciani, *Cross section of the* $^{13}C(\alpha,n)^{16}O$ *reaction at low energies.* PhD thesis, GSSI, 1 2019.

[38] G. F. Knoll, *Radiation Detection and Measurement.* Wiley New York, 2nd ed. ed., 1989.

[39] J. Ziegler. `http://www.srim.org/`. Accessed: 2020-05-12.

[40] "SRIM Uncertainty." `http://www.srim.org/SRIM/SRIMPICS/STOP01/STOP0106.gif`. Accessed: 2020-07-26.

[41] G. R. Gilmore, *Practical Gamma-ray Spectroscopy.* John Wiley & Sons Inc, 2008.

[42] G. Imbriani, H. Costantini, A. Formicola, A. Vomiero, C. Angulo, D. Bemmerer, R. Bonetti, C. Broggini, F. Confortola, P. Corvisiero, J. Cruz, P. Descouvemont, Z. Fulop, G. Gervino, A. Guglielmetti, C. Gustavino, G. Gyürky, A. Jesus, M. Junker, and H. Trautvetter, "S-factor of ^{14}N$(p, \gamma)^{15}$O at astrophysical energies," *European Physical Journal A*, vol. 25, 10 2005.

[43] "Hyperopt." `https://github.com/hyperopt/hyperopt`. Accessed: 2020-06-19.

[44] G. F. Ciani, L. Csedreki, J. Balibrea-Correa, A. Best, M. Aliotta, F. Barile, D. Bemmerer, A. Boeltzig, C. Broggini, C. Bruno, A. Caciolli, F. Cavanna, T. Chillery, P. Colombetti, P. Corvisiero, T. Davinson, R. Depalo, A. Leva, L. Paolo, and S. Zavatarelli, "A new approach to monitor ^{13}C-targets degradation in situ for ^{13}C$(\alpha, n)^{16}$O cross-section measurements at LUNA," *The European Physical Journal A*, vol. 56, 03 2020.

[45] "Scipy." `https://docs.scipy.org/doc/scipy/reference`. Accessed: 2020-06-19.

[46] "MAESTRO." `https://www.ortec-online.com/products/application-software/maestro-mca`. Accessed: 2020-06-19.